Towards an End-to-End Analysis and Prediction System for Weather, Climate, and Marine Applications in the Red Sea

Ibrahim Hoteit[1,*], Yasser Abualnaja[1], Shehzad Afzal[1], Boujemaa Ait-El-Fquih[1], Triantaphyllos Akylas[2], Charls Antony[1], Clint Dawson[3], Khaled Asfahani[4], Robert J. Brewin[5], Luigi Cavaleri[6], Ivana Cerovecki[7], Bruce Cornuelle[7], Srinivas Desamsetti[8], Raju Attada[1], Hari Dasari[1], Jose Sanchez-Garrido[9], Lily Genevier[1], Mohamad El Gharamti[10], John A. Gittings[1], Elamurugu Gokul[1], Ganesh Gopalakrishnan[7], Daquan Guo[1], Bilel Hadri[1], Markus Hadwiger[1], Mohammed Abed Hammoud[1], Myrl Hendershott[7], Mohamad Hittawe[1], Ashok Karumuri[11], Omar Knio[1], Armin Köhl[12], Samuel Kortas[1], George Krokos[1], Ravi Kunchala[13], Leila Issa[14], Issam Lakkis[15], Sabique Langodan[1], Pierre Lermusiaux[2], Thang Luong[1], Jingyi Ma[1], Olivier Le Maitre[16], Matthew Mazloff[7], Samah El Mohtar[1], Vassilis P. Papadopoulos[17], Trevor Platt[18], Larry Pratt[19], Naila Raboudi[1], Marie-Fanny Racault[18], Dionysios E. Raitsos[20], Shanas Razak[1], Sivareddy Sanikommu[1], Shubha Sathyendranath[18], Sarantis Sofianos[20], Aneesh Subramanian[21], Rui Sun[7], Edriss Titi[22,23], Habib Toye[1], George Triantafyllou[17], Kostas Tsiaras[17], Panagiotis Vasou[1], Yesubabu Viswanadhapalli[24], Yixin Wang[1], Fengchao Yao[1], Peng Zhan[1], George Zodiatis[25]

[1] King Abdullah University of Science and Technology (KAUST), Thuwal, Saudi Arabia

[2] Massachusetts Institute of Technology (MIT), Cambridge, Massachusetts, USA

[3] The University of Texas at Austin, Austin, Texas, USA

[4] Saudi Aramco, Damam, Saudi Arabia

[5] University of Exeter, Cornwall, United Kingdom

[*] *Corresponding author*: ibrahim.hoteit@kaust.edu.sa

Early Online Release: This preliminary version has been accepted for publication in *Bulletin of the American Meteorological Society*, may be fully cited, and has been assigned DOI 10.1175/BAMS-D-19-0005.1. The final typeset copyedited article will replace the EOR at the above DOI when it is published.

[6] Institute of Marine Sciences, Venice, Italy

[7] Scripps Institution of Oceanography, La Jolla, California, USA

[8] National Center for Medium Range Weather Forecasting (NCMRWF), Noida, India

[9] University of Malaga, Spain

[10] National Center of Atmospheric Research (NCAR), Boulder, Colorado, USA

[11] University of Hyderabad, Hyderabad, India

[12] University of Hamburg, Hamburg, Germany

[13] Indian Institute of Technology, Delhi, India

[14] Lebanese American University, Beirut, Lebanon

[15] American University of Beirut, Beirut, Lebanon

[16] Ecole Polytechnique, Palaiseau, France

[17] Hellenic Centre for Marine Research (HCMR), Anavissos, Greece

[18] Plymouth Marine Laboratory (PML), Plymouth, United Kingdom

[19] Woods Hole Oceanographic Institution (WHOI), Woods Hole, Massachusetts, USA

[20] National and Kapodistrian University of Athens, Athens, Greece

[21] University of Colorado, Boulder, Colorado, USA

[22] University of Cambridge, Cambridge, United Kingdom

[23]Texas A&M University, College Station, Texas, USA

[24] National Atmospheric Research Laboratories (NARL), Gadanki, India

[25] Coastal & Marine Research Laboratory, Crete, Greece

Accepted for publication in *Bulletin of the American Meteorological Society*. DOI 10.1175/BAMS-D-19-0005.1.

Capsule Summary

An integrated, high resolution, data-driven regional modeling system has been recently developed for the Red Sea region and is being used for research and various environmental applications.

Abstract

The Red Sea, home to the second-longest coral reef system in the world, is a vital resource for the Kingdom of Saudi Arabia. The Red Sea provides 90% of the Kingdom's potable water by desalinization, supporting tourism, shipping, aquaculture and fishing industries, which together contribute about 10-20% of the country's GDP. All these activities, and those elsewhere in the Red Sea region, critically depend on oceanic and atmospheric conditions.

At a time of mega-development projects along the Red Sea coast, and global warming, authorities are working on optimizing the harnessing of environmental resources, including renewable energy, rainwater harvesting, etc. All these require high-resolution weather and climate information. Toward this end, we have undertaken a multi-pronged R&D activity in which we are developing an integrated data-driven regional coupled modeling system. The telescopically-nested components include 5km-600m resolution atmospheric models to address weather and climate challenges, 4km-50m resolution ocean models with regional and coastal configurations to simulate and predict the general and mesoscale circulation; 4km-100m ecosystem models to simulate the biogeochemistry; and 1km-50m resolution wave models. In addition, a complementary probabilistic transport modeling system predicts dispersion of contaminant plumes, oil-spill, and marine ecosystem connectivity. Advanced ensemble data assimilation capabilities have also been implemented for accurate forecasting.

Accepted for publication in *Bulletin of the American Meteorological Society*. DOI 10.1175/BAMS-D-19-0005.1.

Resulting achievements include significant advancement in our understanding of the regional circulation and its connection to the global climate, development and validation of long-term Red Sea regional atmospheric-oceanic-wave reanalyses, and forecasting capacities. These products are being extensively used by academia/government/industry in various weather and marine studies and operations, environmental policies, renewable energy applications, impact assessment, flood-forecasting, etc.

Accepted for publication in *Bulletin of the American Meteorological Society*. DOI 10.1175/BAMS-D-19-0005.1.

1. **Introduction**

The Red Sea is a semi-enclosed, elongated marginal sea, lying between Africa and Asia, connected to the Indian Ocean through the Strait of BaM in the south and to the Mediterranean through the Suez Canal in the north (Fig.1). As a vital resource for fisheries, agriculture, tourism, freshwater through desalination, and a major shipping route, the Red Sea is of paramount political and economic importance for both the region and the world. Influenced by distinct geological, atmospheric, and hydrographic conditions, the Red Sea is a unique LME characterized by the second longest and third largest coral reef system in the world, thriving under one of the warmest and most saline conditions of the world oceans (Edwards and Head 1986). All major oceanographic processes occur in the Red Sea, but at much smaller spatio-temporal scales compared to the global ocean, making it an ideal test basin for studies of climate impact on regional ocean circulations as it is expected to exhibit a faster response to global climate variations (Belkin 2009; Carvalho et al. 2018). Despite its political, economic and scientific importance, the Red Sea remains a vastly under-explored region.

The Red Sea is a geologically young ocean with an average width of 280 km, length of 2000 km, and maximum depths exceeding 2500 m along its axial trench. Extending from 12.5 ºN to 30 ºN in the NW-SE direction, it has a constricted connection with the Gulf of Aden, with a maximum depth of only 137 m at the Hanish Sill. The bathymetry varies from extensive shallow shelves with depths < 50 m in the south to steep-sloped basins with depths > 800 m in the north.

The atmospheric conditions over the Red Sea are mainly influenced by the arid surrounding terrestrial environment, the seasonal Indian monsoon system and the orographic effects of the coastal mountains, with the resultant atmospheric forcing exhibiting marked variability on various time scales (Viswanadhapalli et al. 2017). As a result of the arid climate, the annual mean net

Accepted for publication in *Bulletin of the American Meteorological Society*. DOI 10.1175/BAMS-D-19-0005.1.

freshwater loss due to excess of evaporation over precipitation is estimated at ~2 m yr^{-1}, and the heat flux has a relatively small annual mean heat loss of 11 W m^{-2}, but a large annual cycle with a range of ~200 W m^{-2}. Channeled by the coastal mountains, the surface winds tend to follow the direction of the axis of the Red Sea. In summer (June to September) they generally blow from North-West throughout the whole basin, whereas in winter they reverse from South-East to North-West in the southern Red Sea, creating a convergence zone around 18 °N (Langodan et al. 2014, 2017a). On smaller spatial scales, intense across-basin winds flowing between the coastal mountain gaps are also observed, the most prominent of which is the Tokar jet at around 18 °N of the African coast. This jet is known to generate surface eddies in the Red Sea (Zhai and Bower 2013; Zhan et al. 2018) and to gather moisture from the surface of the Red Sea that can contribute to precipitation over Saudi Arabia and the African Highlands region (Davis et. al. 2017; Dasari et al. 2017). North of 20 °N, the mountain-gap winds usually originate from the Arabian subcontinent and blow westward.

In response to the atmospheric forcing and limited exchanges with the Indian Ocean (Pratt et al. 2000), the Red Sea acts as a concentration basin, producing one of the world's saltiest water masses through a complex two-layer overturning system (Fig.2). In annual mean, an overturning cell occupies the upper layer around the sill depth in the south and deepens to about 300 m in the north. It is composed of a northward surface inflow from the Gulf of Aden and an intermediate southward flow (Sofianos and Johns 2007). This layer is directly subject to the annual cycle of surface heat flux and freshwater loss, resulting in marked seasonal surface temperature variations and a northward increase in surface salinity (Sofianos and Johns 2015). The Red Sea intermediate water is formed in the north during winter and is exported into the Gulf of Aden through BaM, driving a two-layer water exchange (Sofianos and Johns 2007; Zhai et al. 2015). During summer,

Accepted for publication in *Bulletin of the American Meteorological Society*. DOI 10.1175/BAMS-D-19-0005.1.

125 the above overturning circulation and water exchange in the strait reverse, following the onset of
126 the Indian summer monsoon (Yao et al. 2014a,b). An intermediate water intrusion at depths 50 –
127 100 m is induced from the Gulf of Aden, the mean surface currents change to flow southward, and
128 the water exchange in BaM becomes a three-layer structure with the deep outflow significantly
129 suppressed (Patzert 1974; Smeed 1997). The lower layer of the overturning system, extending to
130 the basin bottom, is occupied by a nearly homogeneous warm (~21.5°C) and highly saline (~40.5
131 psu) water mass, referred to as the RSDW. A deep circulation with a southward bottom flow and
132 an intermediate northward return flow centered around a depth of 500 m is suggested by
133 geochemical tracers and dissolved oxygen gradients (Cember 1988; Eshel et al. 1994).

134 Despite being characterized as an oligotrophic LME, the Red Sea is a region of remarkable
135 biodiversity and endemism and hosts one of the world's largest coral reef ecosystems (Carvalho
136 et al. 2018). The Red Sea ecosystem is strongly influenced by environmental conditions, which
137 modulate it on different levels (Triantafyllou et al. 2014). The Red Sea has been subject to warming
138 trends (Raitsos et al. 2011; Chaidez et al. 2017; Krokos et al. 2019) causing coral reef bleaching
139 events (Cantin et al. 2010; Osman et al. 2018; Genevier et al. 2019) and significantly impacting its
140 productivity (Raitsos et al. 2015; Gittings et al. 2018). The Red Sea ecosystem, with its relatively
141 simply-shaped and semi-enclosed basin, high biodiversity and rich dynamics, provides the
142 scientific community with an accessible and ideal natural laboratory to study the physical-
143 biological interactions on multiple spatial and temporal scales.

144 Until recently, the Red Sea region remained largely underdeveloped. The last decade has,
145 however, witnessed an unprecedented increase in population and an acceleration in residential,
146 commercial and industrial developments along the coast. NEOM, short for the Latin-Arabic term
147 Neo-Mustaqbal, signifying "new future", is a $500bn mega-project that aims at building a fully-

Accepted for publication in *Bulletin of the American Meteorological Society*. DOI 10.1175/BAMS-D-19-0005.1.

automated city operating as an independent economic zone in the northwestern part of Saudi Arabia. The RSP is another mega-development along the central Saudi coast and intends to transform the Red Sea coast into a world-class tourist destination, whose blueprint is primarily based on a coastal lagoon with 90-plus pristine islands.

Maintaining a sustainable, healthy marine environment is a core objective of these developments and the Saudi authorities. In this context, understanding and forecasting the regional weather through climate variations is essential for a wide variety of high-impact societal needs, including environmental protection and coastal management, mitigating weather extremes and pollution/contamination, exploration and drilling, accidents response, desalination and plant cooling operations, shipping, harbor management and national security operations, management of fisheries and marine aquaculture, water resources, renewable energy, etc. Given the unique structure of the Red Sea basin and surrounding deserts, and the ocean and atmospheric connections to the global circulation, the need for integrated state-of-the-art modeling and supporting datasets is acute.

Founded in 2009 and located on the shores of the Red Sea, KAUST acts as a hub of frontline research in the biological, physical and geological aspects of the Red Sea region. For this purpose, KAUST dedicated significant resources for studying the Red Sea and understanding its resources, with the goal of preserving its fragile ecosystem while at the same time supporting the local authorities to exploit its unique resources. In parallel to the on-going hydrographic and ecological observational efforts, and through sustained and strong collaborations with many international organizations, the Red Sea Modeling and Prediction group at KAUST has led the development of a comprehensive and integrated modeling and prediction system to study, monitor and predict the atmospheric and oceanic phenomena of the region. The system is being built by

integrating models of atmospheric and oceanic circulations, surface wave, air pollution, dust, and marine biogeochemistry, and developing advanced data analytics and visualization capabilities, achieving remarkable progress in the short span of a decade. The modeling system also relies on *in situ* and remotely-sensed observations (detailed in Table 1) for the purpose of validation and data assimilation and provides insights into the systematic relations between the interactions of different components and the management of various applications.

An important achievement from this effort is the first high-resolution atmospheric reanalysis for the region from 1980 till present, generated using our assimilative atmospheric modeling system, which is turning out to be critical not only for the Red Sea climate research, but also contributing to Indian monsoon studies. This regional reanalysis is being used to force the various ocean and transport models tuned to the Red Sea environment. Notably, these capabilities are currently being extensively used to support various industrial and governmental developments. This review paper elaborates on our state-of-the-art modeling and forecasting technologies, their applications, achievements in science and contributions to industry. It first provides a detailed description of our integrated data-driven Red Sea Modeling system version 1 (iReds-M1). It then catalogues some of our salient science findings and industrial applications using iReds-M1 simulations. It finally lays down our vision for the future development of the system and research directions.

2. **The Integrated Red Sea Model (iReds-M1)**

Accepted for publication in *Bulletin of the American Meteorological Society*. DOI 10.1175/BAMS-D-19-0005.1.

191 iReds-M1 is a comprehensive system comprising a set of state-of-the-art modeling components
192 for simulating the atmosphere, ocean, waves, transports, and bio-geochemistry (as schematized in
193 Fig.3). In its present form, the WRF model is used to force various ocean and transport models.
194 The regional ocean and wave models, based on the MITgcm and WWIII, were further recently
195 fully coupled with WRF (Sun et al., 2019). These regional models are further used to force
196 transport models and to nest very high-resolution coastal ocean models. The system is
197 implemented on the Shaheen-II Cray XC40 – supercomputer at KAUST, a 36-cabinet Cray
198 composed of 6,174 dual socket compute nodes based on 16 core Intel Xeon E5-2698v3 processors
199 running at 2.3GHz, capable of delivering a theoretical peak of 7.2 PFLOP/s (Hadri et al 2015). A
200 description of the components follows.

201 *2.1 The atmospheric models*

202 WRF is a state-of-the-art mesoscale model offering numerous advanced physics options for
203 simulating atmospheric processes at various scales, providing a robust and flexible platform for
204 assimilation (Skamarock et al. 2019). In various baseline studies, WRF successfully reproduced
205 the mean regional climate of the AP and its interannual variability (Viswanadhapalli et al. 2017).
206 It also accurately delineated the structure and climatology of the monsoon low-level jet and
207 monsoon inversion over the Arabian Sea (Viswanadhapalli et al. 2019). We further used long-term
208 WRF simulations to carry out detailed assessments of renewable energy resources in the AP
209 (Langodan et al. 2016a; Dasari et al. 2019a), and for analyzing extreme events (e.g.
210 Viswanadhapalli et al. 2016).

211 We have implemented WRF in assimilation mode at 5-km resolution using the ECMWF
212 global reanalysis as initial and boundary conditions to generate the first high-resolution regional
213 reanalysis for the region from 1980 till present (Viswanadhapalli et al. 2017; Langodan et al.

Accepted for publication in *Bulletin of the American Meteorological Society*. DOI 10.1175/BAMS-D-19-0005.1.

2017a,b). Available satellite and conventional observations in the AP were assimilated (Fig.4). The reanalysis fields are being used to study, for instance, the regional met-ocean conditions (e.g., Viswanadhapalli et al. 2017, 2019), to provide vital information about the background state of the regional environment (e.g., Dasari et al. 2020), and to force our regional ocean models (e.g., Langodan et al. 2014, 2016a; Zhan et al. 2019; Krokos et al. 2020).

To simulate air parcel trajectories as well as transport, dispersion, chemical transformation, and deposition, we use HYSPLIT (Draxler et al. 1997). HYSPLIT, forced with specially-generated WRF forcing at 600 m resolution, was recently used to investigate the distributions of air pollutant concentrations at sites along the Red Sea coast, including the NEOM and RSP regions (Dasari et al. 2020).

2.2. The ocean models

The regional Red Sea circulation is simulated using a 1 km resolution MITgcm (Marshall et al. 1997a,b). The model domain covers the entire Red Sea including the two gulfs (Suez and Aqaba) at the north end, with an open boundary in the Gulf of Aden. The model topography is generated based on the General Bathymetric Chart of the Ocean (Ioc, 2003), updated with available regional data. The eastern open boundary conditions are extracted daily from the global ocean reanalysis GLORYS2. To resolve the different frequencies of water elevation variations (Churchill et al. 2018), the normal velocity at the boundary is adjusted to match the volume flux of GLORYS2. The model is forced with hourly high-resolution WRF downscaled fields, including surface wind, air temperature, specific humidity, precipitation, and downward short-wave and long-wave radiation. The Red Sea MITgcm outputs were validated against different datasets and in various settings and applications (Fig.5). These include studying the general and overturning circulation (Yao et al. 2014a,b), mixed layer variations (Krokos et al. 2020), deep water formation events

(Yao and Hoteit 2018), eddy characteristics (Zhan et al. 2016; 2019), and internal/baroclinic tides (Guo et al. 2018). In addition, the adjoint model of MITgcm is being used to conduct sensitivity studies of quantities-of-interest with respect to the model states and atmospheric forcings (Zhan et al. 2018).

WWIII (Tolman 2008) is used to simulate the waves conditions in the Red Sea at 1 km resolution. The model is configured with 33 frequencies, starting from 0.05 Hz and 36 equally spaced directions and the most recent (ST4) physics formulation (Ardhuin et al. 2010). The extensively validated model outputs (Langodan et al. 2014) were analysed to assess the impact of atmospheric data assimilation on wave predictions (Langodan et al. 2016b), to investigate the physical aspects of the unique seasonally opposing wind-wave systems in the central Red Sea (Langodan et al. 2015), to quantify wave energy potentials (Langodan et al. 2016a), and to study the wind-wave climate and its trends (Langodan et al. 2017a,b; 2018; 2020a).

Transport phenomena are simulated using CMS, a multi-scale probabilistic model of particle dispersal (Paris et al. 2013). CMS, driven by the MITgcm flow fields, has been successfully implemented to study concentrate discharges (Zhan et al. 2015), biological connectivity among different coral reef complexes at coastal (Nanninga et al. 2015), basin (Raitsos et al. 2017), and cross-basin scales (Wang et al. 2019). Oil spill transport and weathering processes are simulated with the well-established MEDSLIK oil spill, trajectory and pollutant transport prediction model (De Dominicis et al. 2013a,b; http://www.oceanography.ucy.ac.cy/medslik/) as Lagrangian particles transported by ocean currents, wind, and waves, and a stochastic displacement that parameterizes turbulent diffusion (Zodiatis et al. 2019).

The marine biogeochemical cycle is simulated using ERSEM (Baretta et al. 1995). ERSEM is a generic comprehensive model that has been successfully implemented across a wide range of

Accepted for publication in *Bulletin of the American Meteorological Society*. DOI 10.1175/BAMS-D-19-0005.1.

coastal and open ocean ecosystems (e.g., Petihakis et al. 2002; Collingridge 2012). It is based on a 'functional' group approach, using size as the major biotic group characteristic. The pelagic model food web consists of four phytoplankton groups, bacteria and three zooplankton groups, and is coupled with the associated benthic model that includes the settling of organic detritus into the benthos and diffusional nutrient fluxes out of the sediment. The pelagic variables include particulate and dissolved organic matter, along with dissolved inorganic nutrients, allowing the coupling of biologically-driven carbon dynamics with the chemical dynamics. ERSEM forced with the outputs of our MITgcm and WRF models outputs has been successfully implemented by Triantafyllou et al. (2014) to describe the main seasonal features of the Red Sea ecosystem.

To simulate complex coastal processes, we implemented ocean models specifically designed for coastal and engineering applications at very high-resolutions O(10 m). These include (i) the Delft3d model (Deltares 2016) to simulate coastal circulation, including flow induced by tides and wind, and sediment transport, (ii) the shallow-water ADCIRC model (Luettich and Westerink 2004) to simulate water level variations and surges on an unstructured grid that enables resolution of near-shoreline detail, and (iii) the SWAN model (Booji et al. 1999) that is coupled with both Delft3D and ADCIRC and designed for simulating short crested waves in coastal environments. These models are forced with high-resolution downscaled WRF fields and are nested within the regional MITgcm and WWIII models.

2.3. Coupled Ocean-atmosphere modeling

Ocean temperatures over the Red Sea region play an important role in modulating the region's weather and climate (Gimeno et al. 2010; Sun et al. 2019). Furthermore, while most of the AP experiences hot and dry summers, the conditions in coastal regions east of the Red Sea are relatively cooler and humid owing to transported moisture from the Red Sea. SKRIPS is a new

Accepted for publication in *Bulletin of the American Meteorological Society*. DOI 10.1175/BAMS-D-19-0005.1.

283 regional coupled ocean-atmosphere WRF+MITgcm+WWIII system that was developed as part of
284 iReds-M1 to study air-sea feedbacks in the Red Sea region and to build long-term regional
285 forecasting capabilities (Sun et al. 2019). Coupling between these components is based on ESMF
286 (Hill et al. 2004) and the interfaces are implemented according to the NUOPC consortium. This
287 regional coupled model allows for oceanic mixed layer heat and momentum to interact with the
288 atmospheric boundary layer dynamics at the mesoscale and higher resolution. This should
289 reproduce feedbacks that cannot be well-resolved by coarse-resolution global coupled models and
290 are absent in regional uncoupled models. SKRIPS was used to investigate the heatwaves in the
291 Red Sea region on seasonal scales, demonstrating that the evolving ocean temperatures
292 considerably improve the prediction of the amplitude of these heatwaves (Fig.6), particularly in
293 the coastal region (Sun et al. 2019).

294 *2.4 Data assimilation*

295 Assimilation is a process by which a model is constrained towards available observations to obtain
296 improved forecasts/hindcasts (Edwards et al., 2015; Hoteit et al., 2018). Our atmospheric and
297 ocean general circulation models are equipped with state-of-the-art assimilation packages; DART
298 (Hoteit et al., 2013), which comprises advanced ensemble schemes (Anderson et al. 2009) and the
299 adjoint-based ECCO-4DVAR system (Stammer et al. 2002; Hoteit et al., 2006) for MITgcm, and
300 the extensive assimilation package of WRF (Barker, 2012), which also includes DART. We are
301 currently employing a cyclic 3DVAR for assimilation with WRF (Viswanadhapalli et al. 2017)
302 and an ensemble adjustment Kalman filter (EAKF) for MITgcm (Toye et al. 2017, 2018). We have
303 recently further developed the DART-MITgcm system to operate with hybrid ensembles
304 composed of flow-dependent and seasonally-varying static members (Toye et al. 2019) and
305 demonstrated significant improvements when driving the MITgcm with ensembles of forcing and

Accepted for publication in *Bulletin of the American Meteorological Society*. DOI 10.1175/BAMS-D-19-0005.1.

physics (Sivareddy et al. 2019). We are currently working on tuning DART for WRF, and on testing newly introduced ensemble assimilation schemes (Hoteit et al. 2015; Raboudi et al. 2018). The system is being further equipped with new efficient techniques for simulating transport phenomena (El-Mohtar et al. 2018) and control of unmanned vehicles (Wang et al. 2017; Albarakati et al. 2019) under the uncertainties described by the ensembles.

We assimilate a variety of observations from different networks, including satellite (e.g. Altimeter SSH and AVHRR SST in the ocean, and QuikSCAT and Advanced Scatterometer winds in the atmosphere) and land-based remote sensing (e.g. weather radars), station-based (e.g. oceanic temperature and salinity observations from moored buoys and ships, meteorological observations from synoptic stations and Metar) and freely drifting (e.g., Argo observations in the ocean, and upper-air soundings of Rawinsonde and pilot balloon) in situ observations. Fig.7 demonstrates the important improvement achieved after ocean assimilation, with significant reduction in the SST and SSH biases in the Red Sea and Gulf of Aden compared to the model free-run. On average, assimilation reduced the forecast RMSEs by 0.5°C for SST and 3 cm for SSH. The assimilated ocean solution is closer to both SST and SSH observations than the corresponding interpolated level-4 products. An operational system for the Red Sea is currently being developed based on a Hybrid ensemble assimilation scheme as part of a project with Saudi Aramco.

2.5 Visualization and data analytics

Advanced visualization is an integral component of our system to support data analysis tasks for scientists and non-expert users. We have developed a visual analytics application, called RedSeaAtlas (Afzal et al. 2019a), considering the tasks, computational and operational requirements of the variety of simulation models and observational datasets of the Red Sea region. The application provides a suite of visualization tools that can facilitate diverse research tasks

Accepted for publication in *Bulletin of the American Meteorological Society*. DOI 10.1175/BAMS-D-19-0005.1.

329 through interactive visual exploration and analysis of spatio-temporal multivariate data (Fig.8).
330 These include interactive feature selection, spatial and temporal filtering, overview and details-on-
331 demand, and capability to analyze data from disparate data sources (Afzal et al. 2019b).

332 We have also developed an interactive visual analysis framework, called Ovis (Höllt et al.
333 2013, 2014), for interactive exploration and analysis of ensemble data. The core components of
334 this framework are constructed based upon an efficient GPU-based computation and visualization
335 pipeline. We presented two case studies to showcase the effectiveness of this framework; the first
336 investigated the placement planning and operation of off-shore structures related to oil and gas
337 industry, and the second demonstrated the effectiveness of this system to plan pathways of
338 autonomous sea vehicles (gliders) through interactive exploration and analysis of ensemble data
339 (Höllt et al. 2013, 2015).

340

341 **3. iReds Salient Contributions to Science and Industry**

342 *3.1 Study of the Red Sea Region Circulation, Climate and Ecosystem*

343 Atmospheric variability: Motivated by the background knowledge from the analysis of global
344 fields, and to meet the need for high-resolution datasets to resolve mesoscale characteristics, we
345 developed a regional reanalysis at 5 km resolution for a 39-year (1980-2018) period (wind details
346 captured by this regional reanalysis are illustrated in Fig.4). The reanalysis fields accurately
347 reproduced the known regional climatic features such as the Red Sea Trough, Red Sea
348 Convergence Zone, Arabian anti-cyclone, and seasonal circulation patterns (Viswanadhapalli et
349 al. 2017). It has been further extensively used to drive iReds ocean models and for subsequent
350 regional applications, and to support the mega-projects being developed along the Red Sea coast.
351 Several studies were also conducted using convective-permitting WRF configurations to

Accepted for publication in *Bulletin of the American Meteorological Society*. DOI 10.1175/BAMS-D-19-0005.1.

352 investigate the predictability of extreme rainfall over the Mecca region, discussed more in detail
353 below.

354 Based on global reanalyses, our study of the regional surface air temperature suggested that
355 it is strongly modulated by the circulation patterns (Attada et al. 2018a), and demonstrated an
356 impact of the Indian summer monsoon through westward propagating Rossby-waves (Attada et al.
357 2018b). Dasari et al. (2017a, 2019b) showed that the baroclinic instability induced by the
358 intensification and southward shift of the subtropical westerly jet over the AP facilitates an
359 increase in the passage of synoptic-transients and winter rainfall. Kunchala et al. (2018; 2019)
360 showed a significant increasing trend in the recent decade in the summer AOD over AP, related to
361 an intensification of the Tokar jet.

362 Ocean general circulation: The Red Sea MITgcm has provided an unprecedented description of
363 the 3D basin circulation and its seasonal and interannual variability. The local buoyancy forcing
364 and Indian monsoon seasonally reverse the basin overturning circulation, and ultimately modulate
365 the water exchanges with the Gulf of Aden through BaM (Yao et al. 2014a,b). Analysis of the
366 interannual variability of the exchanges based on long-term MITgcm simulations forced with the
367 in house high resolution regional Red Sea reanalysis further demonstrated a strong dependence on
368 the intensity and duration of the Indian monsoon (Raitsos et al. 2015; Dreano et al. 2016; Xie et
369 al. 2019). Such simulations also revealed the episodic nature of deep-water renewal related to
370 specific atmospheric events and provided updated estimates of the deep-water renewal time Yao
371 and Hoteit (2018). A 1 km model simulation together was recently analyzed to provide a detailed
372 description of the seasonal and spatial variability of the Red Sea mixed layers (Krokos et al. 2020).
373 The study revealed the dominant role of the air-sea heat fluxes on the mixed layers seasonal

Accepted for publication in *Bulletin of the American Meteorological Society*. DOI 10.1175/BAMS-D-19-0005.1.

variability and the north-south gradient while the effects of extreme evaporation mainly manifest on interannual time scales.

MITgcm-ERSEM-CMS simulations, combined with various remote sensing datasets, have provided new insights into the manner in which physical drivers such as buoyancy fluxes and ocean mixing, and biogeochemical processes drive the ecosystem in the Red Sea. Despite a limited supply of nutrients, their subsurface intrusion from the Gulf of Aden and the winter deep convection drive elevated values of primary productivity in the south during summer (Raitsos et al. 2013; Dreano et al. 2016) and in the north during winter (Gittings et al. 2018). Moreover, marine larvae/planulae disperse nearly passively with the circulation, forming a homogenous genetic connectivity across geographically separated reef sites within most of the basin (Fig.9; Raitsos et al. 2017), except for the southern Red Sea which was suggested to be physically connected with the Indian Ocean (Wang et al. 2019).

Mesoscale circulation: The upper-layer Red Sea circulation is characterized by complex and highly varying mesoscale activity, consisting of energetic semi-permanent and transient eddies, with stronger activity during winter (Zhan et al. 2014). Spatially, the central and northern regions show annual eddy kinetic energy (EKE) peaks during both seasons, with effects on the water column reaching down to 300 m and intensified towards the surface. The MITgcm outputs suggested that the northward gradient of heat loss tilts the isopycnals, which gradually deepen towards the north, thereby enabling baroclinic instabilities and hence the eddy generation (Zhan et al. 2016). The EKE dominates the mean flow kinetic energy (Zhan et al. 2016), with the fate of observed eddies being largely governed by atmospheric forcing and local ocean conditions (Zhan et al. 2018). Driven by considerable heat fluxes, intensified eddy activity promotes convection processes, especially during winter in the north (Papadopoulos et al. 2013; 2015). The northward transport of

Accepted for publication in *Bulletin of the American Meteorological Society*. DOI 10.1175/BAMS-D-19-0005.1.

warmer and fresher water by eddies reduces the intrinsic meridional gradient and flattens the isopycnals, which in turn limits the eddy generation and was interpreted as a typical negative feedback mechanism (Zhan et al. 2019). Based on WRF-MITgcm-CMS simulations, the Red Sea mesoscale circulation was found to play an important role in transporting biogeochemical tracers within the basin (Fig.9) and in supporting the marine ecosystem (Zhan et al. 2014; Dreano et al. 2016; Raitsos et al. 2017; Guo et al., 2020).

Tides: The main tidal signal in the Red Sea propagates from the Arabian Sea through BaM. Observations and simulations suggest a high variability of tidal elevation with latitude, with the northern and southern basins exhibiting relatively large amplitudes compared to the central basin (Guo et al. 2016). Barotropic tides generate internal tides and solitary waves, mainly on the steep sides of the deep trough in the southern part of the Red Sea (da Silva et al. 2012; Guo et al. 2016). Our simulations using a 200 m non-hydrostatic MITgcm and CMS showed that the breaking of internal waves induces vertical mixing, which could increase the supply of nutrients to the euphotic zone and enhance biological productivity, by disrupting the pycnocline and inducing turbulence (Guo et al. 2020).

Waves: Based on long-term WWIII simulations forced with the in-house WRF downscaled Red Sea reanalysis, the wave variability in the Red Sea was naturally associated with the dominant regional wind regimes (Langodan et al. 2014). Although wind intensity in the basin is usually moderate, a prolonged duration and the existence of a long fetch may give rise to waves that reach up to 3.5 m. The irregular shape of the Red Sea coast creates shadowed areas, especially in the south where southward-moving waves reduce to swell and propagate unidirectionally. During summer, consistent northwesterly winds generate mean wave heights of 1-1.5 m in the north, frequently exceeding 2 m (Langodan et al. 2014, 2018). The southward wave system persists

Accepted for publication in *Bulletin of the American Meteorological Society*. DOI 10.1175/BAMS-D-19-0005.1.

420 throughout the year, while the northward system associated with the monsoon winds exhibits a
421 well-defined seasonality between October and April (Langodan et al. 2018). The co-existence of
422 northward and southward waves in winter creates a convergence zone in the central Red Sea
423 (Langodan et al. 2015). Various transversal jets, such as the Tokar jet on the Sudan coast and others
424 that originate in the AP generate locally dominant wave regimes (Langodan et al. 2017b). These
425 exhibit strong seasonality and are usually dominated by other systems.

426 Ecological indicators: The recent development of multi-sensor satellite missions, such as the
427 Ocean Colour Climate Change Initiative (OC-CCI, Sathyendranath et al. 2019), has increased the
428 coverage of surface Chl-a measurements in the Red Sea by enhancing the retrieval of satellite data
429 under adverse atmospheric conditions. Using available in-water measurements of Chl-a, Brewin
430 *et al.* (2013, 2019) and Racault *et al.* (2015) have shown that both standard ocean-colour
431 algorithms and the OC-CCI algorithm perform well in the Red Sea, but further improvements have
432 been achieved by developing a regional algorithm specifically-tuned to the basin (Brewin et al.
433 2015).

434 The analysis of the derived long-term Chl-a dataset together with the MITgcm, WRF, CMS
435 and ERSEM simulations has enabled an unprecedent understanding of the general functioning of
436 the Red Sea ecosystem and its productivity. The open waters of the Red Sea Chl-a exhibit a distinct
437 seasonality with maximum concentrations seen during wintertime, which was attributed to vertical
438 mixing in the north and wind-induced horizontal intrusion of nutrient-rich water in the south, and
439 minimum concentrations during summer (Raitsos et al. 2013). However, large sporadic blooms
440 have been reported during summer in the coastal southern Red Sea driven by the GAIW (Racault
441 et al. 2015; Dreano et al. 2016). The concentration and the duration of the phytoplankton growing
442 season in the Red Sea are modulated by the strength of the winter monsoon over the Arabian Sea,

Accepted for publication in *Bulletin of the American Meteorological Society.* DOI 10.1175/BAMS-D-19-0005.1.

443 which affects the horizontal advection of fertile waters from the Indian Ocean (Raitsos et al.
444 2015). Warmer conditions over the region were also associated with substantially weaker winter
445 phytoplankton blooms, which initiate later and are shorter in their overall duration (~ 4 weeks)
446 (Gittings et al. 2018; Gittings et al. 2019a). Satellite-derived estimates of phytoplankton size
447 structure are in good agreement with the *in situ* measurements, and also capture the spatial
448 variability related to regional mesoscale dynamics (Gittings et al. 2019b). iReds outputs were also
449 used along with in situ and satellite observations to investigate the basin ecological responses to
450 the combined effects of biogeochemical and physical environmental stressors (Ellis et al., 2019).
451
452 *3.2 High-Resolution Nested Modelling in Support of New Mega-Developments along the Red*
453 *Sea Coast*
454 Met-Ocean modeling in NEOM: NEOM spreads over an area of 26,500 km^2 along the northern
455 Red Sea coast of Saudi Arabia, bordering Jordan and Egypt. To support environmental impact
456 assessment efforts and to generate essential met-ocean data required for initial planning, high-
457 resolution atmospheric and oceanic models were implemented and nested within the regional Red
458 Sea models. A 3-year 600 m resolution WRF simulation was performed to investigate the
459 orographic influence on the coastal atmospheric conditions and to drive high-resolution coastal
460 ocean models. Air-quality was also investigated using HYSPLIT driven by the WRF fields to study
461 dispersion of pollutants and their diurnal variations in relation to the land-sea breezes and boundary
462 layer heights (Dasari et al. 2020).
463 The large-scale ocean circulation of the NEOM region simulated by the regional MITgcm
464 suggests numerous eddy features with the topography being the critical factor driving their
465 interactions. A coupled Delft3D+SWAN model configuration with horizontal resolution of 50 m

Accepted for publication in *Bulletin of the American Meteorological Society*. DOI 10.1175/BAMS-D-19-0005.1.

and 10 vertical sigma levels was nested within MITgcm to resolve the coastal circulations and was forced with tides and 600 m WRF fields. Seasonal simulations highlighted different coastal circulation features, including a prominent localized eddy-like structure in the center of the NEOM lagoon where the inner water connects with the open ocean through a narrow channel, and a persistent northwest-southeast current along the broad offshore edge of the coral reefs. The "residence time" estimates based on trajectories of simulated passive particles suggests a faster ventilation rate in winter. The SWAN model nested within the regional WWIII suggested a dominance of locally generated waves in the southeast direction, with a maximum significant wave height of ~0.8 m, associated with consistent strong northwesterlies.

Extreme waves and water levels for KAEC: KAEC is a new city under development along the western Saudi coast, comprising the largest port on the Red Sea, residential districts, and an industrial valley. The area is surrounded by coral reefs and includes a shallow lagoon on its southern side. We supported the development of the sea wall for coastal protection by providing estimates of extreme wave heights and water levels for the KAEC shoreline. For this, we used a coupled ADCIRC+SWAN model configured on a triangular grid with an open boundary in the Arabian Sea. The model's unstructured-grid resolution varied from a maximum vertex spacing of approximately 60 km near the boundary down to 60 m near the KAEC coastline. The bathymetry was generated from 0.5 m resolution LiDAR surveys of the KAEC coast. Simulations were carried out for a 30-year period, forced with the our WRF downscaled atmospheric reanalysis. Extreme value analyses were applied to estimate different return levels of wave heights and water levels. The model effectively simulated the dampening of the offshore waves propagating towards the shoreline by the coral reefs (Fig.10). The KAEC coastline being characterized by a weak tidal regime, extreme sea levels are dominated by meteorological activity, mostly observed during

Accepted for publication in *Bulletin of the American Meteorological Society*. DOI 10.1175/BAMS-D-19-0005.1.

winter. The 100-year return levels of wave heights and water level were estimated at 70 cm and 65 cm, respectively, only marginally (~5 cm) different from the 30-year maxima (Langodan et al. 2020b; Antony et al. 2020).

3.2. Regional Forecasting Applications

Extreme rainfall forecasting: The KSA is characterized by a hot and arid desert climate. Occasionally, extreme precipitation events over the Jeddah region have led to flooding that caused extensive loss of human life and damage to infrastructure (e.g. de Vries et al. 2013). The large-scale features are important factors in producing regional extreme precipitation, which may exceed three times the average annual rainfall. These heavy rainfall events are associated with the northward extension of the Red Sea trough and intensification of the Arabian Anticyclone, which provide warm moist air to the region, creating favorable conditions for the development of a short-lived quasi-stationary mesoscale convective systems (Dasari et al. 2017a). Using a convective-permitting WRF configuration, Viswanadhapalli et al. (2016) assessed the predictability of two extreme rainfall events formed over Jeddah while assimilating various combinations of conventional and satellite observations (Fig.11a). A similar WRF configuration was implemented by Dasari et al. (2017b) to study the Mecca 2016 extreme rainfall event. More recently, Luong et al. (2020) investigated the impact of urbanization using WRF by incorporating an urban canopy model and urban land cover for several extreme weather events over Jeddah showing that urbanization enhanced rainfall by ~25%.

Oil-spill forecasting: iReds is regularly used to support oil spill prediction efforts. As an example, we have supported the Saudi authorities in the southern Red Sea by simulating a realistic oil spill scenario from an abandoned oil tanker filled with oil and anchored at Ras-Isa port north of

Accepted for publication in *Bulletin of the American Meteorological Society*. DOI 10.1175/BAMS-D-19-0005.1.

Hudaydah off the coast of Yemen. The ship, which has not been operational since March 2015, is corroding and there are serious concerns that the gas building up in the storage tanks could lead to an explosion that might trigger an oil spill (Meredith 2019). The tanker carries an estimated volume of 1 million barrels of crude oil, four times the amount of oil released in the 1989 Exxon Valdez oil spill. MEDSLIK was used to model the transport and fate of oil for winter and summer scenarios. Forecast winds, waves and ocean currents generated by iReds during the first two weeks of February and August 2019 have been used as inputs. The oil was continuously released at the tanker location (15° 15' 11" latitude and 42° 36' 52" longitude) over the two-week simulation period. Fig.11b shows the concentration of oil (in barrels km^{-2}) at the end of the simulation period. Following the pattern of the predicted ocean circulation, the oil was transported north-east, where about 60% of its volume washed up onshore. 20% of the remaining oil formed a surface slick of about 55 km^2 in size and the other 20% evaporated.

4. Future Directions

iReds has so far contributed new insights into the regional atmospheric and oceanic circulations, their variability and trends in the Red Sea basin. Outputs from its various long-term simulations established, in particular, a unique basin-wide eddy activity and its driving forces, a prominent seasonally-varying overturning circulation modulated by the Indian monsoon, and the occasional fast ventilation of its deep waters through deep water formation events forced by cold weather anomalies in its northern end. The system was further critically important in supporting the ongoing mega-projects along the Red Sea shores, providing unique information about the regional environment to optimize the design and the operations of these new developments. It further

Accepted for publication in *Bulletin of the American Meteorological Society*. DOI 10.1175/BAMS-D-19-0005.1.

developed for the first time regionally-tuned forecasting capabilities that were successfully tested during urgent environmental situations.

We are envisioning, and have already started working along several directions, to implement new capabilities and continue enhancing iReds performances in the future, while further deepening our understanding of the regional circulation and variability. Our ultimate goal is to develop an integrated data-driven modeling and forecasting system that incorporates all available oceanic and atmospheric observations in the Red Sea region and makes predictions and actionable information available to scientists, government and industry, and non-expert recipients. In this regard, the first Red Sea operational system is expected to be released online during 2021 to provide weekly forecasts of the basin-wide atmospheric (WRF) – oceanic (MITgcm) – wave (WWIII) conditions at 4km, 2km and 1km resolutions, respectively. It will be subsequently equipped with state-of-the-art interactive visualization and data analytics to provide decision makers with real-time access to relevant information. Future work will then focus on (i) equipping iReds with new capabilities for forecasting aerosols (dust and pollution) and the marine biogeochemistry, and (ii) extending the forecasting time-range of the system to subseasonal-to-seasonal and annual scales through a combination of coupled modeling and data assimilation, and spatial-range to the urban and coastal scales through downscaling.

4.1 iReds developments

Beyond the importance of predicting dust and atmospheric pollution, aerosols play a crucial role in the radiation budget and the development of clouds and precipitation. They are also an important source of nutrients for the Red Sea ecosystem. So far, aerosol variations have only been climatologically accounted for in iReds. WRF is equipped with state-of-the-art modules to simulate and study aerosols (WRF-Chem), and we have recently implemented it over the AP. We

557 are currently working on developing high-resolution aerosol emission inventories (natural,
558 anthropogenic, and biogenic) on daily-scales by tuning satellite remote sensing retrieval
559 algorithms with available *in situ* measurements. These will be incorporated/assimilated into WRF-
560 Chem to simulate and predict dust storms and outbreaks of industrial and urban haze pollution.

561 As part of the newly established Center of Excellence for NEOM research at KAUST, our
562 modeling system will be further expanded to investigate oceanic and atmospheric circulations at
563 the urban scales. Work is already underway with external collaborators at Imperial College (UK)
564 and Deltares Institute (Netherlands) to build the required Computational Fluid Dynamics (CFD)
565 algorithms in order to downscale our models' outputs and capabilities at these scales. In this regard,
566 we have further recently introduced and successfully tested a new dynamical downscaling
567 algorithm with WRF, based on the Continuous Data Assimilation approach (Desamsetti et al.
568 2019). Downscaling ensembles from the global operational centers remain computationally
569 demanding in terms of both computational cost and storage. We will investigate novel approaches
570 for identifying efficient downscaling of probabilistic maps through machine and dynamical
571 learning approaches.

572 In terms of data assimilation, we will continue working on enhancing the skills of our
573 ensemble system. In particular, proper accounting of model errors, for instance, through stochastic
574 perturbations and forcing ensembles greatly enhanced the assimilation results. Developing data-
575 driven approaches for quantifying the uncertainties of such perturbations and eventually estimating
576 their parameters as part of the assimilation process is our next target. To extend the time-range of
577 the system predictability, we will also strongly couple the WRF- and MITgcm-DART ensemble
578 assimilation systems to simultaneously exploit the observations of both components.

579 *5. General circulation and climate of the Red Sea and their impact on the ecosystem*

Accepted for publication in *Bulletin of the American Meteorological Society*. DOI 10.1175/BAMS-D-19-0005.1.

While the upper general circulation of the Red Sea is now relatively well-understood, little is still known about the deep circulation. Based on chemical tracers, it has been suggested that a deep overturning cell is present, but our ongoing investigations suggest a more complex 3D circulation with the existence of a basin-wide cyclonic gyre in addition to the deep overturning circulation. Insight into the variability and ventilation of the RSDW is needed to advance our understanding of the general circulation of the Red Sea. We are further implementing non-hydrostatic configurations of the MITgcm with variable-resolution curvilinear grids zooming (~100m) on the straits to resolve in more detail the features of the water exchange with the Indian Ocean through BaM and the water formation and sinking in the north.

Monitoring the decadal and seasonal variability of Red Sea ecosystem indicators, in relation to the regional environmental conditions and broader climate change, is a necessity for the sustainability of marine life and responsible stewardship of its socio-economical assets. Toward this end, we have synergistically combined remotely-sensed ocean-color observations with our models' simulations to investigate various aspects of the Red Sea ecosystem in this historically data-sparse region. Remote sensing will continue to be an integral component of our system, providing information for model validation and assimilation, and predicting how the ecosystem indicators would respond to a changing climate. Currently, we are also developing regionally-tuned algorithms for high-resolution satellite sensors (<300m resolution) that would be particularly useful for tackling ecological issues in the coastal economic zone of the Red Sea. In parallel, we will generate interannual simulations with the ecosystem model, which has been only investigated so far with climatological physical forcing. This multidisciplinary approach is expected to offer new insights into the past and current environmental status of the Red Sea coastal zone, and help us to identify vulnerable regions as well as biodiversity hotspots.

Accepted for publication in *Bulletin of the American Meteorological Society*. DOI 10.1175/BAMS-D-19-0005.1.

6. *Coupled processes, predictability and forecasting at seasonal and climate scales*

The capabilities of the newly developed SKRIPS coupled model are yet to be fully exploited. We will intensify studies using this system to understand coupled phenomena in the Red Sea region at short- and long-term scales, and how those respond to the global climate dynamics and variations. We are currently examining the outputs of the ocean-waves coupling component to investigate wave-currents interactions and coastal circulations, with particular interest in the water-exchanges near and over the coral reefs. Another proposed development of SKRIPS is the coupling of the atmospheric chemical and marine ecosystem components to investigate regional carbon variations and exchanges.

This coupled system will be at the core of building long-term regional predictive capabilities at the subseasonal-to-seasonal through climate scales by downscaling global forecasts and climate change scenarios. We will assess the system predictability of the regional phenomenon at different scales, including extreme weather events (heavy rainfall, air and marine heatwaves). The focus will be on identifying key factors and dynamical processes that may provide extended predictability for the region and on quantifying their impact on the forecasting skills through sensitivity studies. These will be then used as a guide for designing efficient, regionally-tuned, data-driven strategies for projecting the weather and climate of the Red Sea and their impact on the regional ecosystem and Red Sea coast.

Acknowledgments

Dedicated to the bright memory of Professor Trevor Platt, a pioneer in biological oceanography and a key contributor to Red Sea research.

Accepted for publication in *Bulletin of the American Meteorological Society*. DOI 10.1175/BAMS-D-19-0005.1.

625 The development of the Red Sea modeling system is being supported by the Virtual Red Sea
626 Initiative and the Competitive Research Grants (CRG) program from the Office of Sponsored
627 Research at KAUST, Saudi Aramco Company through the Saudi ARAMCO Marine
628 Environmental Center at KAUST, and by funds from KAEC, NEOM and RSP through Beacon
629 Development Company at KAUST.
630

Accepted for publication in *Bulletin of the American Meteorological Society*. DOI 10.1175/BAMS-D-19-0005.1.

631 **List of Acronyms and Abbreviations**

3DVAR	Three-Dimensional Variational Data Assimilation
4DVAR	Four-Dimensional Variational Data Assimilation
ADCIRC	Advanced CIRCulation
AMSU	Advanced Microwave Sounding Unit
AOD	Aerosol Optical Depth
AP	Arabian Peninsula
APHRODITE	Asian Precipitation - Highly-Resolved Observational Data Integration Towards Evaluation
ASCAT	Advanced SCATterometer
AVHRR	Advanced Very-High-Resolution Radiometer
AWS	Automatic Weather Station
BaM	Bab-al-Mandeb
CCMP	Cross-Calibrated Multi-Platform
AMSU	Advanced Microwave Sounding Unit
ASCAT	Advanced SCATterometer
AVISO	Archiving, Validation and Interpretation of Satellite Oceanographic data
Chl-a	Chlorophyll-a
CFD	Computational Fluid Dynamics
CMEMS-L4	Copernicus Marine Environment Monitoring Service
CMORPH	Climate prediction center MORPHing
CMS	Connectivity Modelling System
CRU	Climatic Research Unit
DART	Data Assimilation Research Testbed
DWR	Doppler Weather Radar
EAKF	Ensemble Adjustment Kalman Filter
ECCO	Estimating the Circulation and Climate of the Ocean
ECCO2	Estimating the Circulation and Climate of the Ocean, Phase II
ECMWF	European Center for Medium-Range Weather Forecasts
EKE	Eddy Kinetic Energy
ERA	ECMWF Re-Analysis
ERSEM	European Regional Seas Ecosystem Model
ESA	European Space Agency
ESMF	Earth System Modeling Framework
FNL	Final Analysis
GAIW	Gulf of Aden Intrusion Water
GDP	Gross Domestic Product
GHRSST	Group for High Resolution Sea Surface Temperature (GHRSST)

Accepted for publication in *Bulletin of the American Meteorological Society*. DOI 10.1175/BAMS-D-19-0005.1.

GLORYS2	GLobal Ocean ReanalYSis 2
GPSRO	Global Position System Radio Occultation
HYCOM	HYbrid Coordinate Ocean Model
HYSPLIT	Hybrid Single-Particle Lagrangian Integrated Trajectory
iReds-M1	integrated data-driven Red Sea Modeling system version 1
KAEC	King Abdullah Economic City
KAUST	King Abdullah University of Science and Technology
KSA	Kingdom of Saudi Arabia
LME	Large Marine Ecosystem
MITgcm	Massachusetts Institute of Technology general circulation model
NCEP	National Centers for Environmental Prediction
NUOPC	National United Operational Prediction Capability
OC-CCI	Ocean Colour Climate Change Initiative
OLCI	Ocean and Land Color Instrument
OSTIA	Operational Sea Surface Temperature and Sea Ice Analysis
OTIS	Ohio state university Tidal Inversion Software
PME	Presidency of Meteorology and Environment
RADS	Radar Altimeter Database
RMSE	Root-Mean-Square-Error
RSDW	Red Sea Deep Water
RSOW	Red Sea Outflow Water
RSP	Red Sea Project
SKRIPS	Scripps-KAUST Regional Integrated Prediction System
SSH	Sea Surface Height
SST	Sea Surface Temperature
SWAN	Simulating WAves Nearshore
TRMM	Tropical Rainfall Measuring Mission
WHOI	Woods Hole Oceanographic Institution
WOA	World Ocean Atlas
WRF	Weather Research and Forecasting
WWIII	WaveWatch-III

632

Accepted for publication in *Bulletin of the American Meteorological Society*. DOI 10.1175/BAMS-D-19-0005.1.

633 **References**

634 Afzal, S., M. Hittawe, S. Ghani, T. Jamil, O. Knio, M. Hadwiger, and I. Hoteit, 2019a: The state
635 of the art in visual analysis approaches for ocean and atmospheric datasets. Computer
636 Graphics Forum, 38: 881-907.

637 Afzal, S., S. Ghani, G. Tissington, S. Langodan, H. P. Dasari, D. Raitsos, J. Gittings, T. Jamil, M.
638 Srinivasan, and I. Hoteit, 2019b: RedSeaAtlas: A visual analytics tool for spatio-temporal
639 multivariate data of the Red Sea. Workshop on Visualization in Environmental Sciences
640 (EnvirVis), doi:10.2312/envirvis.20191101.

641 Albarakati, S., R. M. Lima, L. Giraldi, I. Hoteit, and O. Knio, 2019: Optimal 3D trajectory planning
642 for AUVs using ocean general circulation models. Ocean Engineering, 188, 106266.

643 Anderson, J., T. Hoar, K. Raeder, H. Liu, N. Collins, R. Torn, and A. Avellano, 2009: The Data
644 Assimilation Research Testbed: A community dacility. Bull. Amer. Meteor. Soc., 90, 1283-
645 1296.

646 Antony, C., S. Langodan, P. R. Shanas, H. P. Dasari, Y. Abualnaja, O. Knio, and I. Hoteit, 2019:
647 Modelling extreme water levels along the central Red Sea coast of Saudi Arabia-Processes
648 and frequency analysis. Natural Hazards, under review.

649 Ardhuin, F., E. Rogers, V. Babanin, J. F. Filipot, A. Roland, A. Van der Westhuysen, P.
650 Queffeoulou, J. M. Lefevre, A. Lotfi, and F. Collard, 2010: Semiempirical dissipation
651 source functions for ocean waves. Part I: Definition, calibration and validation. J. Phys.
652 Oceanogr., 40, 1917-1941.

Accepted for publication in *Bulletin of the American Meteorological Society*. DOI 10.1175/BAMS-D-19-0005.1.

653 Attada, R., H. P. Dasari, J. S. Chowdary, Y. Ramesh Kumar, O. Knio, and I. Hoteit, 2018a: Surface
654 air temperature variability over the Arabian Peninsula and its links to circulation patterns.
655 Int. J. Climatol., 39(1), 445-464.

656 Attada R., H. P. Dasari, A. Parekh, J. S. Chowdary, S. Langodan, O. Knio, and I. Hoteit, 2018b:
657 The role of the Indian Summer Monsoon variability on Arabian Peninsula summer climate.
658 Clim. Dyn., 52, 3389.

659 Attada, R., K. Ravi Kumar, Y. Ramesh Kumar, H. P. Dasari, O. Knio, and I. Hoteit, 2018c:
660 Prominent modes of summer surface air temperature variability and associated circulation
661 anomalies over the Arabian Peninsula. Atmos. Sci. Lett., 19:e860,
662 https://doi.org/10.1002/asl.860.

663 Baretta, J. W., W. Ebenhoh, and P. Ruardij, 1995: The European-Regional-Seas-Ecosystem-
664 Model, a complex marine ecosystem model. Neth. J. Sea Res., 33, 233-246.

665 Barker, D., X.-Y. Huang, Z. Liu, T. Auligné, X. Zhang, S. Rugg, R. Ajjaji, A. Bourgeois, J. Bray,
666 Y. Chen, M. Demirtas, Y.-R. Guo, T. Henderson, W. Huang, H.-C. Lin, J. Michalakes, S.
667 Rizvi, and X. Zhang, 2012: The Weather Research and Forecasting Model's Community
668 Variational/Ensemble Data Assimilation System: WRFDA. Bull. Amer. Meteor. Soc., 93,
669 831–843.

670 Belkin, I. M., 2009: Rapid warming of Large Marine Ecosystems. Prog. Oceanogr., 81, 207–213.

671 Booij, N., R. C. Ris, and L. H. Holthuijsen, 1999: A third-generation wave model for coastal
672 regions. Part 1: Model description and validation. J. Geophys. Res., 104, 7649-7666.

Accepted for publication in *Bulletin of the American Meteorological Society*. DOI 10.1175/BAMS-D-19-0005.1.

673 Bower, A. S., and J. T. Farrar, 2015: Air–Sea Interaction and Horizontal Circulation in the Red
674 Sea. N.M.A. Rasul and I.C.F. Stewart, Eds., Vol. 1900 of Springer Earth System Sciences,
675 Springer Berlin Heidelberg, 329-342.

676 Brewin B., X. A. G. Morán, D. E. Raitsos, J. Gittings, M. L. Calleja, M. S. Viegas, M. I. Ansari,
677 N. Al-Otaibi, T. M. Huete-Stauffer, and I. Hoteit, 2019: Factors regulating the relationship
678 between total and size-fractionated chlorophyll-a in coastal waters of the Red Sea. Frontiers
679 in Microbiology, 10, 1964.

680 Brewin, R. J. W., D. E. Raitsos, G. Dall'Olmo, N. Zarokanellos, T. Jackson, M-F. Racault, E. S.
681 Boss, S. Sathyendranath, B. H. Jones, and I. Hoteit, 2015: Regional ocean-colour
682 chlorophyll algorithms for the Red Sea. Remote Sensing of Environment, 162, 257-270.

683 Brewin, R. J. W., D. E. Raitsos, Y. Pradhan, and I. Hoteit, 2013: Comparison of chlorophyll in the
684 Red Sea derived from MODIS-Aqua and in vivo fluorescence. Remote Sensing of
685 Environment, 136, 218-224.

686 Cantin, N. E., A. L. Cohen, K. B. Karnauskas, A. M. Tarrant, and D. C. McCorkle, 2010: Ocean
687 warming slows coral growth in the central Red Sea. Science, 329, 322-325.

688 Carvalho, S., B. Kürten, G. Krokos, I. Hoteit, and J. Ellis, 2018: The Red Sea. Book Chapter in
689 World Seas: An Environmental Evaluation – vol.II: the Indian Ocean to the Pacific, Chapter
690 3, 49-74.

691 Cember, R. P. 1988: On the sources, formation, and circulation of Red Sea deep water. J. Geophys.
692 Res., 93, 8175-8191.

693 Chaidez, V., D. Dreano, S. Agusti, C. M. Duarte, and I. Hoteit, 2017: Decadal trends in Red Sea
694 maximum surface temperature. Sci. Rep., 7, 8144.

Accepted for publication in *Bulletin of the American Meteorological Society*. DOI 10.1175/BAMS-D-19-0005.1.

695 Churchill, J. H., Y. Abualnaja, R. Limeburner, and M. Nellayaputhenpeedika, 2018: The dynamics
696 of weather-band sea level variations in the Red Sea. Regional Studies in Marine Science, 24,
697 336-342.

698 Collingridge, K., 2012: Modelling risk areas in the North Sea for blooms of the invasive comb
699 jellyfish Mnemiopsis Leidyi. CEFAS Summer Proj., 9, 21-36.

700 da Silva, J., J. Magalhaes, T. Gerkema, and L. Maas, 2012: Internal solitary waves in the Red Sea:
701 An unfolding mystery. Oceanography, 25, 96-107.

702 Dasari, H. P., L. Sabique, V. Yesubabu, V. B. Rao, V. P. Papadopoulos, and I. Hoteit, 2017a:
703 ENSO influence on the Red Sea Convergence Zone and Associated Rainfall. Int. J.
704 Climatol., doi:10.1002/joc.5208.

705 Dasari, H. P., A. Raju, O. Knio, and I. Hoteit, 2017b: Analysis of a severe weather event over
706 Mecca, Kingdom of Saudi Arabia using observations and high-resolution modeling.
707 Meteorological Applications, doi:10.1002/met.1662.

708 Dasari, H. P., S. Desamsetti, S. Langodan, R. Attada, R. K. Kunchala, Y. Viswanadhapalli, O.
709 Knio, and I. Hoteit, 2019a: High-resolution assessment of solar energy resources over the
710 Arabian Peninsula. Applied Energy, 248, 354-371.

711 Dasari, H. P., D. Srinivas, S. Langodan, R. Attada, A. Karumuri, and I. Hoteit, 2019b:
712 Multidecadal variability of the Arabian Peninsula rainfall and its relationship with the
713 ENSO signals in the tropical Indo-Pacific. J. Climate, under revision.

714 Dasari, H. P., S. Desamsetti, S. Langodan, S. Singh, L. N. K. Ramakrishna, and I. Hoteit, 2020:
715 Air-quality assessment over NEOM, Kingdom of Saudi Arabia. Atmospheric Environment,
716 230, doi:10.1016/j.atmosenv.2020.117489.

Accepted for publication in *Bulletin of the American Meteorological Society*. DOI 10.1175/BAMS-D-19-0005.1.

717

718 Davis, S. R., L. J. Pratt and H. Jiang, 2015: The Tokar Gap: Regional circulation, diurnal
719 variability, and moisture transport based on numerical simulations. J. Climate, 28, 5585-
720 5907.

721 De Dominicis, M., N. Pinardi, G. Zodiatis, and R. Lardner, 2013b: MEDSLIK-II, a Lagrangian
722 marine surface oil spill model for short-term forecasting - Part I: Theory. Geosci. Model.
723 Dev., 6, 1851-1869.

724 De Dominicis, M., N. Pinardi, G. Zodiatis, and R. Archetti, 2013a: MEDSLIK-II, a Lagrangian
725 marine surface oil spill model for short-term forecasting - Part II: Numerical simulations
726 and validations. Geosci. Model. Dev., 6, 1871-1888.

727 de Vries, A. J., E. Tyrlis, D. Edry, S. O. Krichak, B. Steil, and J. Lelieveld, 2013: Extreme
728 precipitation events in the Middle East: Dynamics of the Active Red Sea Trough. J.
729 Geophys. Res., 118, 7087-7108.

730 Deltares, 2016: Delft3D-FLOW. Simulation of multi-dimensional hydrodynamic flow and
731 transport phenomena, including sediments – User Manual, Version 3.15, Deltares, Delft,
732 The Netherlands.

733 Desamsetti, S., H. P. Dasari, S. Langodan, E. S. Titi, O. Knio, and I. Hoteit, 2019: Efficient
734 dynamical downscaling of general circulation models Using continuous data assimilation.
735 Q. J. Roy. Meteor. Soc., 245, 3175-3194.

736 Draxler, R. R., and G. D. Hess, 1997: Description of the HYSPLIT_4 modeling system. NOAA
737 Tech. Memo. ERL ARL-224, NOAA/Air Resources Laboratory, Silver Spring, MD, 24 pp.

Accepted for publication in *Bulletin of the American Meteorological Society*. DOI 10.1175/BAMS-D-19-0005.1.

738 Dreano, D., D. E. Raitsos, J. Gittings, G. Krokos, and I. Hoteit, 2016: The Gulf of Aden
739 intermediate water intrusion regulates the Southern Red Sea summer phytoplankton blooms.
740 PLoS One, 11(12), e0168440.

741 Edwards, A., and S. Head, 1986: Red Sea key environment. Headington Hill Hall, Oxford, UK:
742 Pergamon Press.

743 Edwards, C., A. Moore, I. Hoteit, and B. Cornuelle, 2015: Regional ocean data assimilation.
744 Annual Review of Marine Science, 7, 21-42.

745 Ellis, J.I., T. Jamil, H. Anlauf, D.J. Coker, J. Curdia, J. Hewitt, B.H. Jones, G. Krokos, B. Kurten,
746 H.D. Prasad, F. Rooth, S. Carvalho, and I. Hoteit, 2019: Multiple stressor effects on coral
747 reef ecosystems. Global Change Biology, 25(12), 4131-4146.

748 El Mohtar, S., I. Hoteit, O. Knio, L. Issa, and I. Lakkis, 2018: Lagrangian tracking in stochastic
749 fields with application to an ensemble of velocity fields in the Red Sea. Ocean Modelling,
750 131, 1-14.

751 Eshel, G., M. A. Cane, and M. B. Blumenthal, 1994: Modes of subsurface, intermediate, and deep
752 water renewal in the Red Sea. J. Geophys. Res., 99, 15941-15952.

753 Genevier, L. G. C., T. Jamil, D. E. Raitsos, G. Krokos, and I. Hoteit, 2019: Marine heatwaves
754 reveal coral reef zones susceptible to bleaching in the Red Sea. Global Change Biol, 25,
755 2338-2351.

756 Gimeno, L., A. Drumond, R. Nieto, R. M. Trigo, and A. Stohl, 2010: On the origin of continental
757 precipitation. Geophys. Res. Let., 37(13), doi:10.1029/2010GL043712.

758 Gittings, J. A., D. E. Raitsos, G. Krokos, and I. Hoteit, 2018: Impacts of warming on phytoplankton
759 abundance and phenology in a typical tropical marine ecosystem. Sci. Rep., 8, 2240.

Accepted for publication in *Bulletin of the American Meteorological Society*. DOI 10.1175/BAMS-D-19-0005.1.

760 Gittings J. A., R. J. W. Brewin, D. E. Raitsos, M. Kheireddine, M. Ouhssain, B. H. Johns, and I.
761 Hoteit, 2019a: Remotely sensing phytoplankton size structure in the Red Sea. Remote
762 Sensing of Environment, 234, 111387.

763 Gittings, J. A., D. E. Raitsos, M. Kheireddine, M. F. Racault, H. Claustre, and I. Hoteit, 2019b:
764 Evaluating tropical phytoplankton phenology metrics using contemporary tools. Sci. Rep.,
765 9, 674.

766 Guo, D. Q., T. R. Akylas, P. Zhan, A. Kartadikaria, and I. Hoteit, 2016: On the generation and
767 evolution of internal solitary waves in the southern Red Sea. J. Geophys. Res., 121, 8566-
768 8584.

769 Guo, D. Q., A. Kartadikaria, P. Zhan, J. S. Xie, M. J. Li, and I. Hoteit, 2018: Baroclinic tides
770 simulation in the Red Sea: comparison to observations and basic characteristics. J. Geophys.
771 Res., 123, 9389-9404.

772 Guo, D., P. Zhan, and I. Hoteit 2020: Numerical study of shoaling process of internal solitary
773 waves in the southern Red Sea. Journal of Geophysical Research, under revision.

774 Hadri, B., S. Kortas, S. Feki, R. Khurram, and G. Newby, 2015: Overview of the KAUST's Cray
775 X40 system–Shaheen II. Proceedings of the 2015 Cray User Group.

776 Hill, C., C. DeLuca, Balaji, M. Suarez, and A. Silva, 2004: The architecture of the earth system
777 modeling framework. Comp. Sci. Eng., 6, 18-28.

778 Höllt, T., A. Magdy, G. Chen, G. Gopalakrishnan, I. Hoteit, C. D. Hansen, and M. Hadwiger,
779 2013: Visual Analysis of uncertainties in ocean forecasts for planning and operation of off-
780 Shore structures. IEEE Pacific Visualization Symposium, pp. 59-66.

Accepted for publication in *Bulletin of the American Meteorological Society*. DOI 10.1175/BAMS-D-19-0005.1.

781 Höllt, T., A. Magdy, P. Zhan, G. Chen, G. Gopalakrishnan, I. Hoteit, C.D. Hansen, and M.
782 Hadwiger, 2014: Ovis: A Framework for Visual Analysis of Ocean Forecast Ensembles.
783 IEEE Transactions on Visualization and Computer Graphics, 20, 1114-1126.

784 Höllt, T., M. Hadwiger, O. Knio, and I. Hoteit, 2015: Probability maps for the visualization of
785 assimilation ensemble flow data. Workshop on Visualization in Environmental Sciences
786 (EnvirVis), pp.43-47.

787 Hoteit, I., B. Cornuelle, A. Köhl, and D. Stammer: Treating strong adjoint sensitivities in tropical
788 eddy-permitting variational data assimilation, 2006: Q. J. Roy. Meteor. Soc., 131, 3659-
789 3682.

790 Hoteit, I., T. Hoar, G. Gopalakrishnan, J. Anderson, N. Collins, B. Cornuelle, A. Kohl, and P.
791 Heimbach, 2013: A MITgcm/DART ocean prediction and analysis system with application
792 to the Gulf of Mexico. Dynamics of Atmospheres and Oceans, 63, 1-23.

793 Hoteit, I., D. T. Pham, M. E. Gharamti and X. Luo, 2015: Mitigating observation perturbation
794 sampling errors in the stochastic EnKF. Mon. Wea. Rev., 143, 2918-2936.

795 Hoteit, I., X. Luo, M. Bocquet, A. Kohl, and B. Ait-El-Fquih, 2018: Data Assimilation in
796 Oceanography: Current Status and New Directions. Book Chapter, New Frontiers in
797 Operational Oceanography, Editors: E. P. Chassignet, A. Pascual, J. Tintore, and J. Verron,
798 GODAE Ocean View, 815pp, https://doi.org/10.17125/gov2018.

799 Ioc, I., 2003: BODC 2003 - Centenary Edition of the GEBCO Digital Atlas, published on CD-
800 ROM on behalf of the Intergovernmental Oceanographic Commission and the International
801 Hydrographic Organization as part of the General Bathymetric Chart of the Oceans, British
802 oceanographic data centre, Liverpool.

Accepted for publication in *Bulletin of the American Meteorological Society*. DOI 10.1175/BAMS-D-19-0005.1.

803 Krokos, G., V. P. Papadopoulos, S. S. Sofianos, H. Ombao, P. Dybczak, and I. Hoteit, 2019:
804 Natural climate oscillations may counteract Red Sea warming over the coming decades.
805 Geophys. Res. Lett., 46, 3454-3461.

806 G. Krokos, I. Cerovecki, P. Zhan, M. C. Hendershott, I. Hoteit (2020). Seasonal Evolution of
807 Mixed Layers in the Red Sea and the Relative Contribution of Atmospheric Buoyancy and
808 Momentum Forcing. Journal of Geophysical Research, under review, 2020

809 Kunchala, R., R. Attada, H. P. Dasari, V. R. Kumar, S. Langodan, Y. Abualnaja, and I. Hoteit,
810 2018: Aerosol optical depth variability over the Arabian Peninsula using satellite and
811 ground based observations. Atmospheric Environment, 187, 346-357.

812 Kunchala, R. K., R. Attada, H. P. Dasari, K. Ramesh, Y. Abualnaja, K. Ashok, and I. Hoteit, 2019:
813 On the recent amplification of dust over the Arabian Peninsula during 2002-2012. J.
814 Geophys. Res., doi: 10.1029/2019JD030695.

815 Langodan, S., L. Cavaleri, Y. Viswanadhapalli, and I. Hoteit, 2014: The Red Sea: a natural
816 laboratory for wind and wave modeling. J. Phys. Oceanogr. 44, 3139-3159.

817 Langodan, S., L. Cavaleri, Y. Viswanadhapalli, and I. Hoteit, 2015: Wind-wave source functions
818 in opposing seas. J. Geoph. Res., 120, 6751-6768.

819 Langodan, S., Y. Viswanadhapalli, H. P. Dasari, O. Knio, and I. Hoteit, 2016a: A high
820 resolution assessment of wind and wave energy potentials in the Red Sea. Applied
821 Energy, 181, 244-255.

822 Langodan, S., V. Yesubabu, and I. Hoteit, 2016b: Impact of atmospheric data assimilation on
823 waves in the Red Sea. Ocean Engineering, 116, 200-215.

Accepted for publication in *Bulletin of the American Meteorological Society*. DOI 10.1175/BAMS-D-19-0005.1.

824 Langodan, S., L. Cavaleri, A. Pomaro, V. Yesubabu, L. Bertotti, and I. Hoteit, 2017a: The
825 climatology of the Red Sea – Part 1: The winds. Int. J. Climatol., 37, 4518-4528.
826 Langodan, S., L. Cavaleri, A. Pomaro, V. Yesubabu, L. Bertotti, and I. Hoteit, 2017b: The
827 climatology of the Red Sea – Part 2: The waves. Int. J. Climatol., 37, 4518-4528.
828 Langodan, S., L. Cavaleri, A. Pomaro, J. Portilla, Y. Abualnaja, and I. Hoteit, 2018: Unraveling
829 climatic wind and wave trends in the Red Sea using wave spectra partitioning. J. Climate,
830 31, 1881-1895.
831 Langodan, S., L. Cavaleri, J. Portilla, Y. Abualnaja, and I. Hoteit, 2020a: Can we extrapolate
832 climate in an inner basin? The case of the Red Sea. Global and Planetary Change, 188,
833 103151.
834 Langodan, S., C. Antony, P.R. Shanas, H. P. Dasari, Y. Abualnaja, O. Knio, and I. Hoteit,
835 2020b: Wave modeling of a reef-sheltered coastal zone in the Red Sea. Ocean Engineering,
836 207, 107378.
837 Luettich, R.A., and J. J. Westerink, 2004: Formulation and numerical implementation of the 2D/3D
838 ADCIRC finite element model Version 44.XX. ADCIRC Tech. Rep., 74 pp.
839 Luong, T. M., H. P. Dasari, and I. Hoteit, 2019: Impact of urbanization on the simulation of
840 extreme rainfall in Jeddah, Saudi Arabia. Journal of Applied Meteorology and Climatology,
841 5, 952-971.
842 Marshall, J., A. Adcroft, C. Hill, L. Perelman, and C. Heisey, 1997a: A finite-volume,
843 incompressible Navier Stokes model for studies of the ocean on parallel computers. J.
844 Geophys. Res., 102, 5753-5766.

Accepted for publication in *Bulletin of the American Meteorological Society*. DOI 10.1175/BAMS-D-19-0005.1.

845 Marshall, J., C. Hill, L. Perelman, and A. Adcroft, 1997b: Hydrostatic, quasi-hydrostatic, and
846 nonhydrostatic ocean modeling. J. Geophys. Res., 102, 5733-5752.

847 Meredith, S., 2019: 'Floating bomb': Decaying oil tanker near Yemen coast could soon explode,
848 experts warn. CNBC, 24 July 2019, https://www.cnbc.com/2019/07/24/oil-tanker-near-
849 yemen-coast-could-soon-explode-experts-warn.html, accessed on 12 December 2019.

850 Nanninga, G. B., P. Saenz-Agudelo, P. Zhan, I. Hoteit, and M. L. Berumen, 2015: Not finding
851 Nemo: limited reef-scale retention in a coral reef fish. Coral Reefs, 34, 383-392.

852 Osman, E. O., D. J. Smith, M. Ziegler, B. Kürten, C. Conrad, K. M. El- Haddad, C.R. Voolstra,
853 and D. J. Suggett, 2018: Thermal refugia against coral bleaching throughout the northern
854 Red Sea. Global Change Biology, 24, 474-484.

855 Papadopoulos, V. P., Y. Abualnaja, S. A. Josey, A. S. Bower, D. E. Raitsos, H. Kontoyiannis, and
856 I. Hoteit, 2013: Atmospheric forcing of the winter air–sea heat fluxes over the northern Red
857 Sea. J. Clim., 26, 1685-1701.

858 Papadopoulos, V.P., P. Zhan, S.S. Sofianos, D.E. Raitsos, M. Qurban, Y. Abualnaja, A. Bower,
859 H. Kontoyiannis, A. Pavlidou, T. T. Mohamed Asharaf, N. Zarokanellos, and I. Hoteit,
860 2015: Factors governing the deep ventilation of the Red Sea. J. Geophys. Res., Oceans, 120,
861 7493-7505.

862 Paris, C. B., J. Helgers, E. van Sebille, and A. Srinivasan, 2013: Connectivity Modeling System:
863 A probabilistic modeling tool for the multi-scale tracking of biotic and abiotic variability in
864 the ocean. Environ. Modell. Softw., 42, 47-54.

865 Patzert, W. C., 1974: Wind induced reversal in the Red Sea circulation. Deep-Sea Res., 21, 109-
866 121.

Accepted for publication in *Bulletin of the American Meteorological Society*. DOI 10.1175/BAMS-D-19-0005.1.

867 Petihakis, G., G. Triantafyllou, I. J. Allen, I. Hoteit, and C. Dounas, 2002: Modelling the spatial
868 and temporal variability of the Cretan Sea ecosystem. J. Mar. Sys., 36, 173-196.

869 Pratt, L. J., H. E. Deese, S. P. Murray and W. Johns, 2000: Continuous dynamical nodes in straits
870 having arbitrary cross sections, with applications to the Bab-al-Mandab. J. Phys. Oceanogr.,
871 30, 2515-2534.

872 Raboudi, N. F., B. Ait-El-Fquih, and I. Hoteit, 2018: Ensemble Kalman filtering with one-step-
873 ahead smoothing. Mon. Wea. Rev., 146, 561-581.

874 Racault, M.-F., D. E. Raitsos, M. L. Berumen, R. J. W. Brewin, T. Platt, S. Sathyendranath, and I.
875 Hoteit, 2015: Phytoplankton phenology indices in coral reef ecosystems: Application to
876 ocean-color observations in the Red Sea. Remote Sensing of Environment, 160, 222-234.

877 Raitsos, D. E., I. Hoteit, P. K. Prihartato, T. Chronis, G. Triantafyllou, and Y. Abualnaja, 2011:
878 Abrupt warming of the Red Sea. Geophys. Res. Lett., 38, doi:10.1029/2011GL047984.

879 Raitsos, D. E., Y. Pradhan, R. J. W. Brewin, G. Stenchikov, and I. Hoteit, 2013: Remote sensing
880 the phytoplankton seasonal succession of the Red Sea. PLoS One, 8, e64909,
881 doi:10.1371/journal.pone.0064909.

882 Raitsos, D. E., X. Yi, T. Platt, M.-F. Racault, R.J.W. Brewin, Y. Pradhan, V.P. Papadopoulos, S.
883 Sathyendranath, and I. Hoteit, 2015: Monsoon oscillations regulate fertility of the Red Sea.
884 Geophys. Res. Lett., 42, 855-862.

885 Raitsos, D. E., R. J. W. Brewin, P. Zhan, D. Dreano, Y. Pradhan, G. B. Nanninga, and I. Hoteit,
886 2017: Sensing coral reef connectivity pathways from space. Sci. Rep., 7, 9338.

887 Ralston, D. K., H. Jiang, and T. F. Ferrar, 2013: Waves in Red Sea: Response to monsoonal and
888 mountain gap winds. Continental Shelf Research, 65, 1-13.

Accepted for publication in *Bulletin of the American Meteorological Society*. DOI 10.1175/BAMS-D-19-0005.1.

889 Sathyendranath, S., R.J.W. Brewin, C. Brockmann, V. Brotas, B. Calton, A. Chuprin, P. Cipollini,
890 A.B. Couto, J. Dingle, R. Doerffer, C. Donlon, M. Dowell, A. Farman, M. Grant, A. Groom,
891 A. Horseman, T. Jackson, H. Krasemann, S. Lavender, V. Martinez-Vicente, C. Mazeran,
892 F. Mélin, T.S. Moore, D. Müller, P. Regner, S. Roy, C.J. Steele, F. Steinmetz, J. Swinton,
893 M. Taberner, A. Thompson, A. Valente, M. Zühlke, V.E. Brando, H. Feng, G. Feldman,
894 B.A. Franz, R. Frouin, R.W. Gould, S.B. Hooker, M. Kahru, S. Kratzer, B.G. Mitchell, F.
895 Muller-Karger, H.M. Sosik, K.J. Voss, J. Werdell, amd T. Platt, 2019: An ocean-colour time
896 series for use in climate studies: the experience of the Ocean-Colour Climate Change
897 Initiative (OC-CCI). Sensors, 19, 4285.

898 Sivareddy, S., H. Toye, P. Zhan, S. Langodan, G. Krokos, O. Knio, and I. Hoteit, 2019: Impact of
899 Atmospheric and Model Physics Perturbations on a High-Resolution Ensemble Data
900 Assimilation System of the Red Sea. Journal of Geophysical research, under review.

901 Skamarock, W. C., J. B. Klemp, J. Dudhia, D. O. Gill, Z. Liu, J. Berner, W. Wang, J. G. Powers,
902 M. G. Duda, D. M. Barker, and X.-Y. Huang, 2019: A Description of the Advanced
903 Research WRF Version 4. NCAR Tech. Note NCAR/TN-556+STR, 145 pp.
904 doi:10.5065/1dfh-6p97.

905 Smeed, D., 1997: Seasonal variation of the flow in the strait of Bab-al-Mandab. Oceanol. Acta,
906 20, 773-781.

907 Sofianos, S., and W. E. Johns, 2007: Observations of the summer Red Sea circulation. J. Geophys.
908 Res., 112, 1-20.

909 Sofianos, S., and W. E. Johns, 2015: The Red Sea: Water mass formation, Overturning Circulation,
910 and the Exchange of the Red Sea with the Adjacent Basins. (N. M. A. Rasul & I. C. F.
911 Stewart, Eds.). Berlin, Heidelberg: Springer Berlin Heidelberg.

Accepted for publication in *Bulletin of the American Meteorological Society*. DOI 10.1175/BAMS-D-19-0005.1.

912 Stammer, D., C. Wunsch, R. Giering, C. Eckert, P. Heimbach, J. Marotzke, A. Adcroft, C. N. Hill,
913 and J. Marshall, 2002: The global ocean circulation during 1992–1997, estimated from
914 ocean observations and a general circulation model. J. Geophys. Res., 107, 3118.

915 Sun, R., A. C. Subramanian, A. J. Miller, M. R. Mazloff, I. Hoteit, and B. D. Cornuelle, 2019:
916 SKRIPS v1. 0: a regional coupled ocean-atmosphere modeling framework (MITgcm-WRF)
917 using ESMF/NUOPC, description and preliminary results for the Red Sea. Geosci. Model.
918 Dev., 12, 4221-4244.

919 Tolman, H. L., 2008: User manual and system documentation of WAVEWATCH-III version 3.14.
920 Technical Note Nr.268, pp.25-32, NOAA/NWS/NCEP/OMB.

921 Toye, H., P. Zhan, G. Gopalakrishnan, A. R. Kartadikaria, H. Huang, O. Knio, and I. Hoteit, 2017:
922 Ensemble data assimilation in the Red Sea: sensitivity to ensemble selection and
923 atmospheric forcing. Ocean Dynamics, 67, 915-933.

924 Toye, H., S. Kortas, P. Zhan, and I. Hoteit, 2018: A fault-tolerant HPC scheduler extension for
925 large and operational ensemble data assimilation: Application to the Red Sea. J. Comp. Sci.,
926 27, 46-56.

927 Toye, H., S. Sivareddy, N. Raboudi, and I. Hoteit, 2019: A Hybrid ensemble data assimilation
928 system for the Red Sea: Implementation and Evaluation. Q. J. R. Meteo. Soc., under review.

929 Triantafyllou, G., F. Yao, G. Petihakis, K. Tsiaras, D. E. Raitsos, and I. Hoteit, 2014: Exploring
930 the Red Sea seasonal ecosystem functioning using a three-dimensional biophysical model.
931 J. Geophys. Res., 119, 1791-1811.

Accepted for publication in *Bulletin of the American Meteorological Society*. DOI 10.1175/BAMS-D-19-0005.1.

932 Viswanadhapalli, Y., C. V. Srinivas, S. Langodan, and I. Hoteit, 2016: Predicting extreme rainfall
933 events over Jeddah, Saudi Arabia: impact of data assimilation with conventional and
934 satellite observations. Q. J. Roy. Meteor. Soc., 142, 327-348.

935 Viswanadhapalli, Y., H. P. Dasari, S. Langodan, V. S. Challa, and I. Hoteit, 2017: Climatic
936 features of the Red Sea from a regional assimilative model. Int. J. Climatol., 37, 2563-2581.

937 Viswanadhapalli, Y., H. P. Dasari, S. Dwivedi, V. R. Madineni, S. Langodan, and I. Hoteit, 2019:
938 Variability of monsoon low- level jet and associated rainfall over India. Int. J. Climatol.,
939 doi:10.1002/joc.6256.

940 Wang, T., Le Maître, I. Hoteit, and O. Knio, 2016: Path planning in uncertain flow fields using
941 ensemble method. Ocean Dynamics, 66, 1231-1251.

942 Wang, Y., D. E. Raitsos, G. Krokos, J. A. Gittings, P. Zhan, and I. Hoteit, 2019: Physical
943 connectivity simulations reveal dynamic linkages between coral reefs in the southern Red
944 Sea and the Indian Ocean. Sci. Rep., 9, 16598.

945 Xie, J. S., G. Krokos, S. Sofianos, and I. Hoteit, 2019: Interannual Variability of the Exchange
946 Flow Through the Strait of Bab-al-Mandeb. J. Geophys. Res., 124, 1988-2009.

947 Yao, F. C., I. Hoteit, L. J. Pratt, A. S. Bower, A. Köhl, G. Gopalakrishnan, and D. Rivas, 2014a:
948 Seasonal overturning circulation in the Red Sea. Part-II: Winter circulation. J. Geophys.
949 Res., 119, 2263-2289.

950 Yao, F. C., I. Hoteit, L. J. Pratt, A. S. Bower, P. Zhai, A. Köhl, and G. Gopalakrishnan, 2014b:
951 Seasonal overturning circulation in the Red Sea. Part-I: Model validation and summer
952 circulation. J. Geophys. Res., 119, 2238-2262.

Accepted for publication in *Bulletin of the American Meteorological Society*. DOI 10.1175/BAMS-D-19-0005.1.

953 Yao, F., and I. Hoteit, 2018: Rapid red sea deep water renewals caused by volcanic eruptions and
954 the north Atlantic oscillation. Science advances, 4(6), eaar5637.

955 Zhai, P., and A. S. Bower, 2013: The response of the Red Sea to a strong wind jet near the Tokar
956 Gap in summer. J. Geophys. Res. Oceans, 118, 422-434.

957 Zhai, P., A.S. Bower, W.M. Smlethie Jr., and L.J. Pratt, 2015: Formation and spreading of Red
958 Sea Outflow Water in the Red Sea, J. Geophys. Res., Oceans, 120, 6542-6563.

959 Zhan, P., A. C. Subramanian, F. C. Yao, and I. Hoteit, 2014: Eddies in the Red Sea: A statistical
960 and dynamical study. J. Geophys. Res., 119, 3909-3925.

961 Zhan, P., F. Yao, A. R. Kartadikaria, Y. Viswanadhapalli, G. Gopalakrishnan, and I. Hoteit, 2015:
962 Far-Field ocean conditions and concentrate discharges modeling along the Saudi coast of
963 the Red Sea. Environ. Sci. Eng., 501-520, doi:10.1007/978-3-319-13203-7-21.

964 Zhan, P., A. C. Subramanian, F. C. Yao, A. R. Kartadikaria, D. Q. Guo, and I. Hoteit, 2016: The
965 eddy kinetic energy budget in the Red Sea. J. Geophys. Res., 121, 4732-4747.

966 Zhan, P., G. Gopalakrishnan, A. C. Subramanian, D. Guo, and I. Hoteit, 2018: Sensitivity Studies
967 of the Red Sea Eddies Using Adjoint Method. J. Geophys. Res., 123, 8329-8345.

968 Zhan, P., G. Krokos, D. Guo, and I. Hoteit, 2019: Three-Dimensional Signature of the Red Sea
969 Eddies and Eddy-Induced Transport. Geophys. Res. Lett., 46, 2167-2177.

970 Zodiatis, G., R. Lardner, T. M. Alves, Y. Krestenitis, L. Perivoliotis, S. Sofianos and K.
971 Spanoudaki, 2019: Oil spill forecasting (prediction) in: THE SEA. The Science of Ocean
972 Prediction, Yale University, Number 17, 923-953.

973

974

Accepted for publication in *Bulletin of the American Meteorological Society*. DOI 10.1175/BAMS-D-19-0005.1.

975 Table 1. A variety of *in situ* and satellite observations, and reanalysis datasets are being used to
976 study the regional ocean and atmospheric variabilities and changes, to validate our models,
977 for prescribing model boundary conditions, and for initialization and assimilation. We have
978 also developed regionally-tuned remote sensing algorithms, based on local observations,
979 to generate improved Chlorophyll datasets for the Red Sea region (Brewin et al., 2019).
980 Details of the datasets, and their use, are listed in the Table below.

Datasets and observations	**Type**	**Usage**
Atmospheric Datasets		
ERA-Interim, NCEP FNL, Real-time Global SST, CCMP, CRU	Reanalyses	Initialization and Boundaries
AMSU, QuikSCAT, ASCAT, GPSRO	Satellite	
TRMM, CMORPH, APHRODITE	Rainfall reanalysis	Model validation
Rain gauge precipitation, AWS-PME, KSA Saudi Aramco, KSA RADAR, PME, KSA KAUST-WHOI BUOY Synoptic and Upper - Uni. of Wyoming	Local Met-Ocean	Assimilation and validation
Globwave altimeter wave data	Significant wave height	Wave model validation
Oceanic Datasets		
ECCO2, WOA, GLORYS2	Reanalyses	Initialization and Boundaries
AVHRR, RADS	Satellite	Assimilation and validation
RSP, NEOM, Saudi Aramco Tidal Gauges, KAUST-WHOI BUOY	In-situ Observations	Model validation
OSTIA, AVISO	Satellite	
OTIS	Simulation	Tidal forcing
ESA: Ocean Colour Climate Change Initiative – OC-CCI and Sentinel-3 OLCI	Satellite	Ocean colour / Ecological Indicators

981

982

Accepted for publication in *Bulletin of the American Meteorological Society*. DOI 10.1175/BAMS-D-19-0005.1.

983 **Figures**
984

985

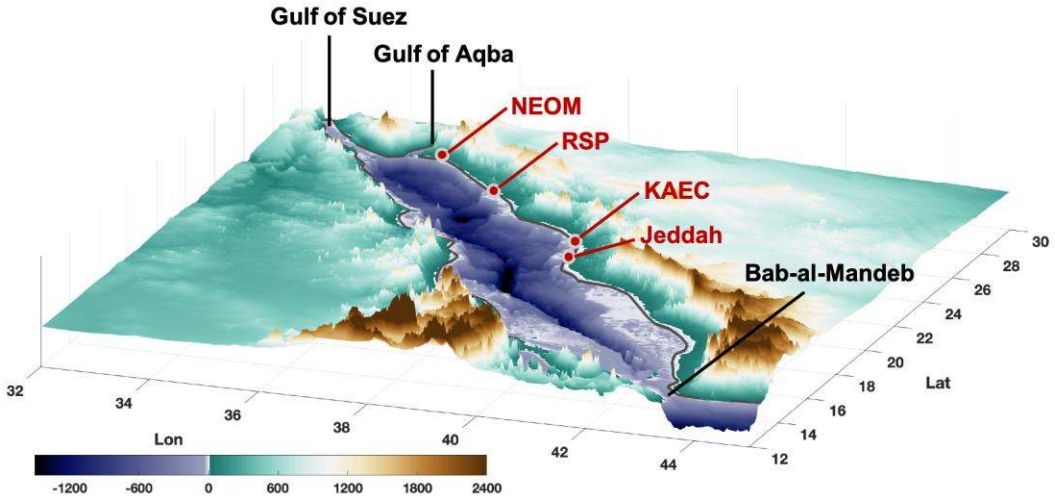

986

987 Figure 1. Topography of the Red Sea region. The important sites along the Saudi coastline are

988 indicated on the map.

989

990

Accepted for publication in *Bulletin of the American Meteorological Society*. DOI 10.1175/BAMS-D-19-0005.1.

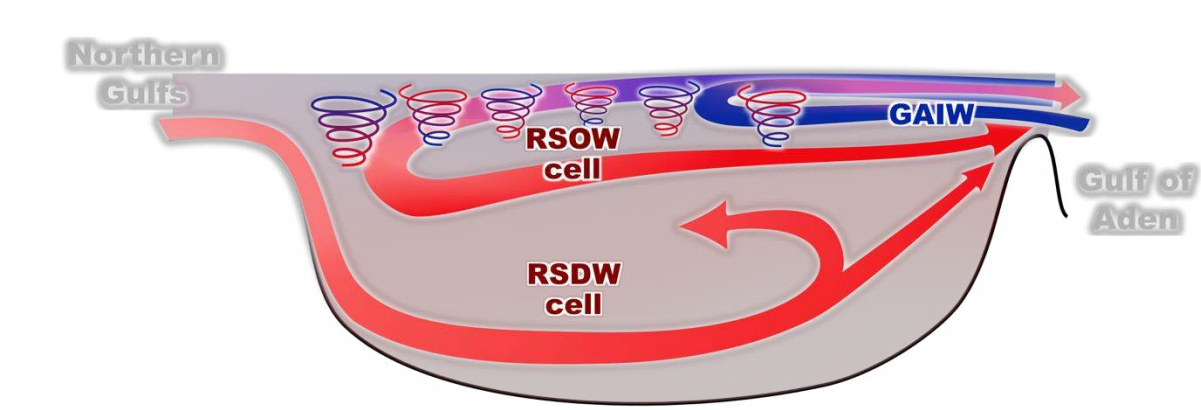

Figure 2. Schematic representation of the main thermohaline cells in the Red Sea circulation (Carvalho et al., 2018). Blue colors represent fresher waters while red colors saline and denser water masses. Mesoscale features, cyclonic and anti-cyclonic eddies, are represented by spirals. RSOW, RSDW and GAIW respectively stand the for Red Sea Outlflow Water, Red Sea Deep Water and Gulf of Aden Intrusion Water.

Accepted for publication in *Bulletin of the American Meteorological Society*. DOI 10.1175/BAMS-D-19-0005.1.

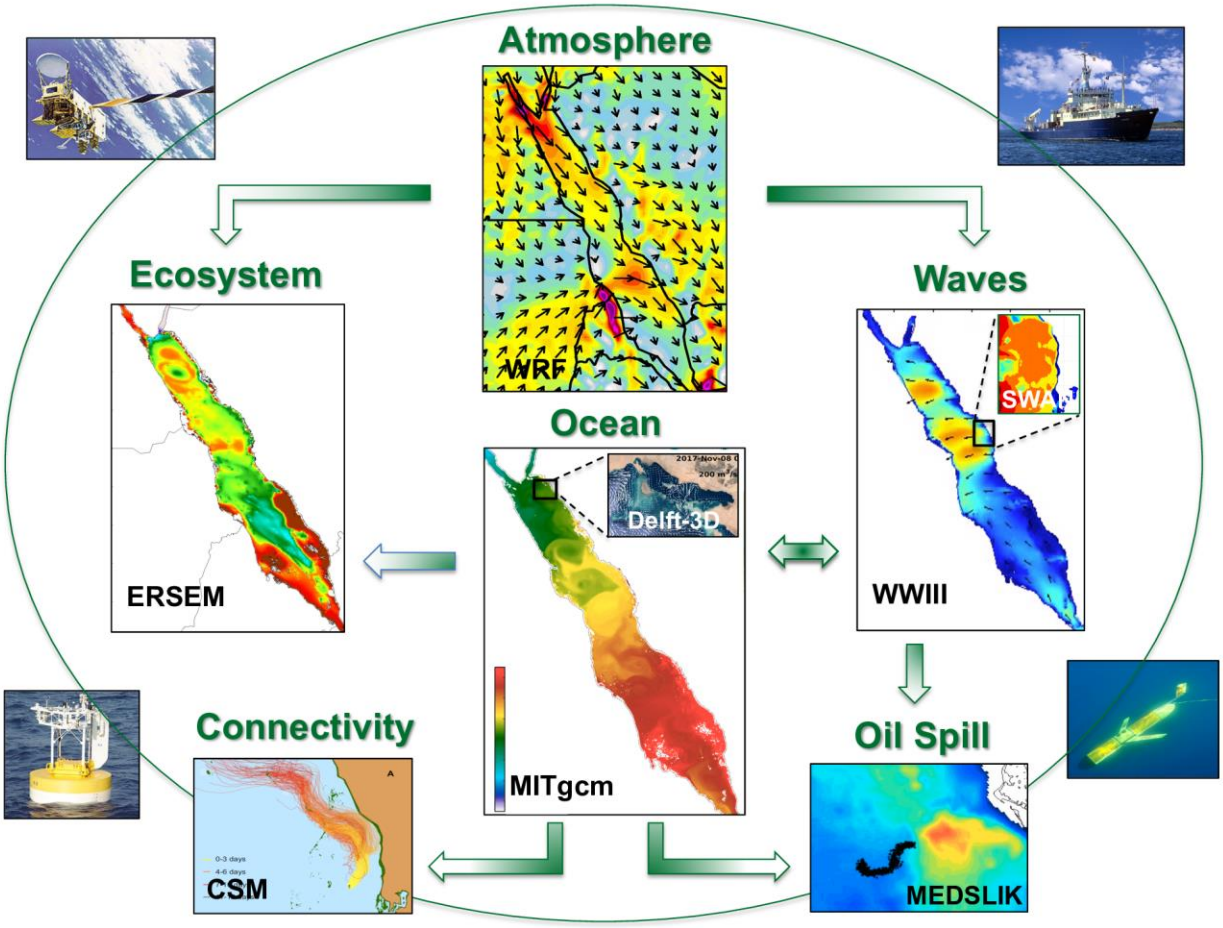

1002 Figure 3. Schematic illustration of the data-driven Red Sea modelling and prediction system
1003 (iReds-M1). Two-way arrows signify two-way coupling, and one-way arrows represent
1004 forcing of uncoupled components. The Atmosphere panel shows mean wind speeds during
1005 the month of July from 5 km WRF Red Sea reanalysis. The Ocean panel shows a sea
1006 surface temperature snapshot in September with the upper-corner subpanel displaying the
1007 volume transport in the upper layer of a high-resolution coastal nesting exercise in the
1008 NEOM region. The Ecosystem panel shows the simulated near-surface Chlorophyll-a
1009 during the winter-mixing period (January-March). The Waves panel shows a significant
1010 wave heights and mean wave directions snapshot in January with the upper-corner
1011 subpanel displaying the distribution of maximum significant wave heights estimated from

Accepted for publication in *Bulletin of the American Meteorological Society*. DOI 10.1175/BAMS-D-19-0005.1.

1012 a high-resolution nested coastal model long-run covering the KAEC region. The
1013 Connectivity and Oil spill panels show simulations of oil and virtual larvae trajectories
1014 released in the central Red Sea.
1015

Accepted for publication in *Bulletin of the American Meteorological Society*. DOI 10.1175/BAMS-D-19-0005.1.

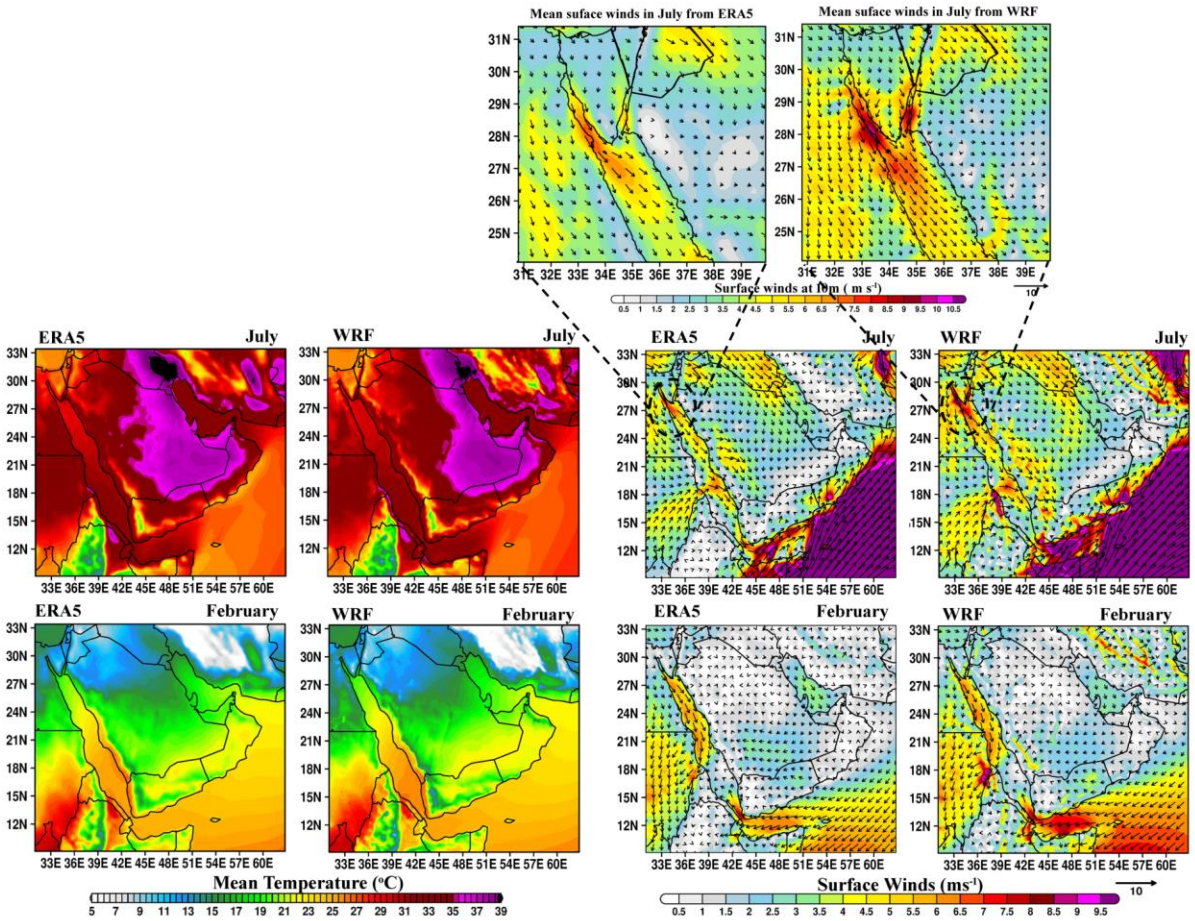

Figure 4. Lower panels show the spatial distribution of summer (July - top panels) and winter (February - bottom panels) months climatology of air temperature at 2 m height, and winds at 10 m height from the 5 km Red Sea reanalysis compared against ERA5 reanalysis. The Red Sea reanalysis reproduces well the main regional winds features in summer and winter, in good agreement with ERA5 reanalysis. The upper two panels zoom over the northern Red Sea region to emphasize the wind features captured by the high-resolution Red Sea reanalysis winds.

Accepted for publication in *Bulletin of the American Meteorological Society*. DOI 10.1175/BAMS-D-19-0005.1.

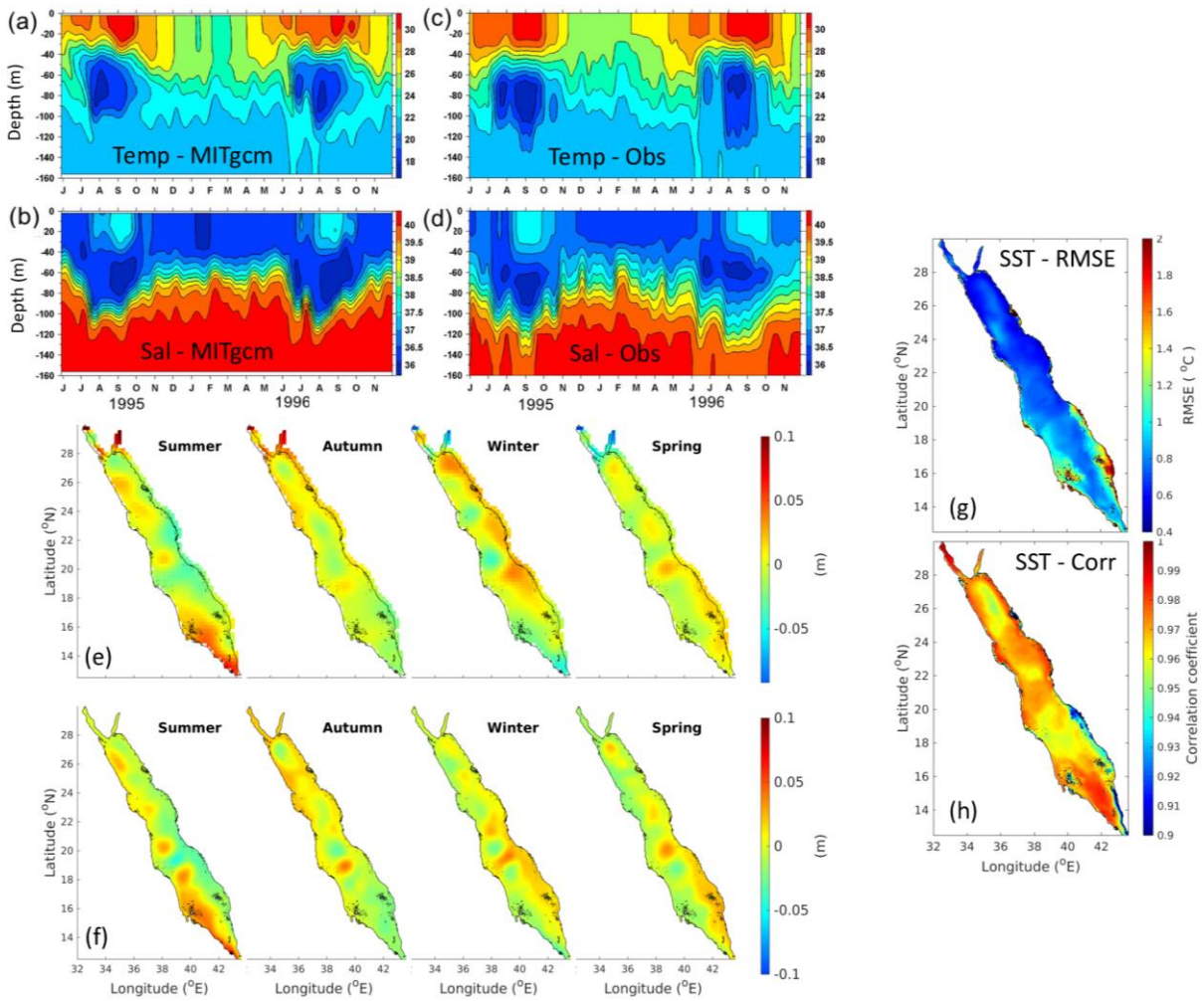

Figure 5. *Upper panel*s (a-d): Hovmöller diagrams (time versus water depth) of (a and c) temperature (°C) and (b and d) salinity (psu) at the Hanish Sill, from June 1995 to November 1996, after filtering with a 20- day low- pass filter. (a) and (b) show 400m resolution southern Red Sea MITgcm simulations taken from Xie et al. (2019) and (c) and (d) display in situ observations. *Lower panels* (e-f): Seasonal climatology of sea level anomaly derived from (e) satellite altimetry data (AVISO) and (f) 1 km MITgcm for the period 2001-2015, in summer (June-August), autumn (Sep-Nov), winter (Dec- Feb) and spring (March-May). *Right panels*: (g) RMSE and (h) correlation coefficient between satellite derived SST (OSTIA) and 1 km daily MITgcm SST, time averaged over the model

Accepted for publication in *Bulletin of the American Meteorological Society*. DOI 10.1175/BAMS-D-19-0005.1.

simulation period 2001-2015. MITgcm successfully reproduces the main features of the general circulation of the Red Sea.

Accepted for publication in *Bulletin of the American Meteorological Society*. DOI 10.1175/BAMS-D-19-0005.1.

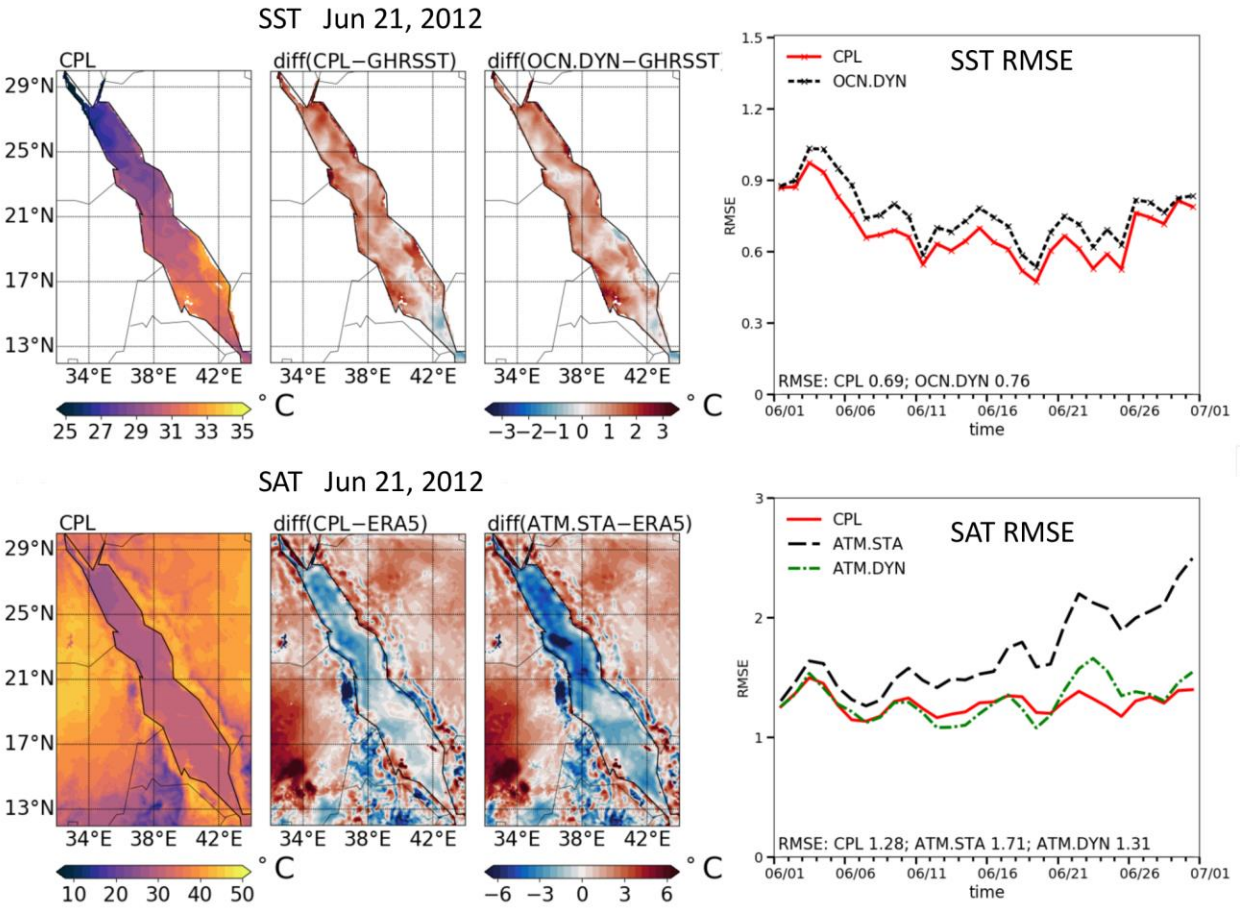

Figure 6. Upper and lower panels respectively show validation results for sea surface temperature (SST) and surface air temperature (SAT) as simulated by the coupled SKRIPS model (Sun et al., 2019). CPL, OCN.DYN, ATM.STA, ATM.DYN denote the coupled WRF-MITgcm run, MITgcm-only driven by ERA5, WRF-only run driven by persistent HYCOM SST, WRF-only run driven by time-varying HYCOM SST, respectively. SST is compared against GHRSST and SAT against ERA5. The simulation initial time is 0000 UTC Jun 01 2012 for all runs. Coupled and uncoupled runs well simulate SST and SAT in the Red Sea region with smaller RMSEs from the coupled simulation compared to the validation data.

Accepted for publication in *Bulletin of the American Meteorological Society*. DOI 10.1175/BAMS-D-19-0005.1.

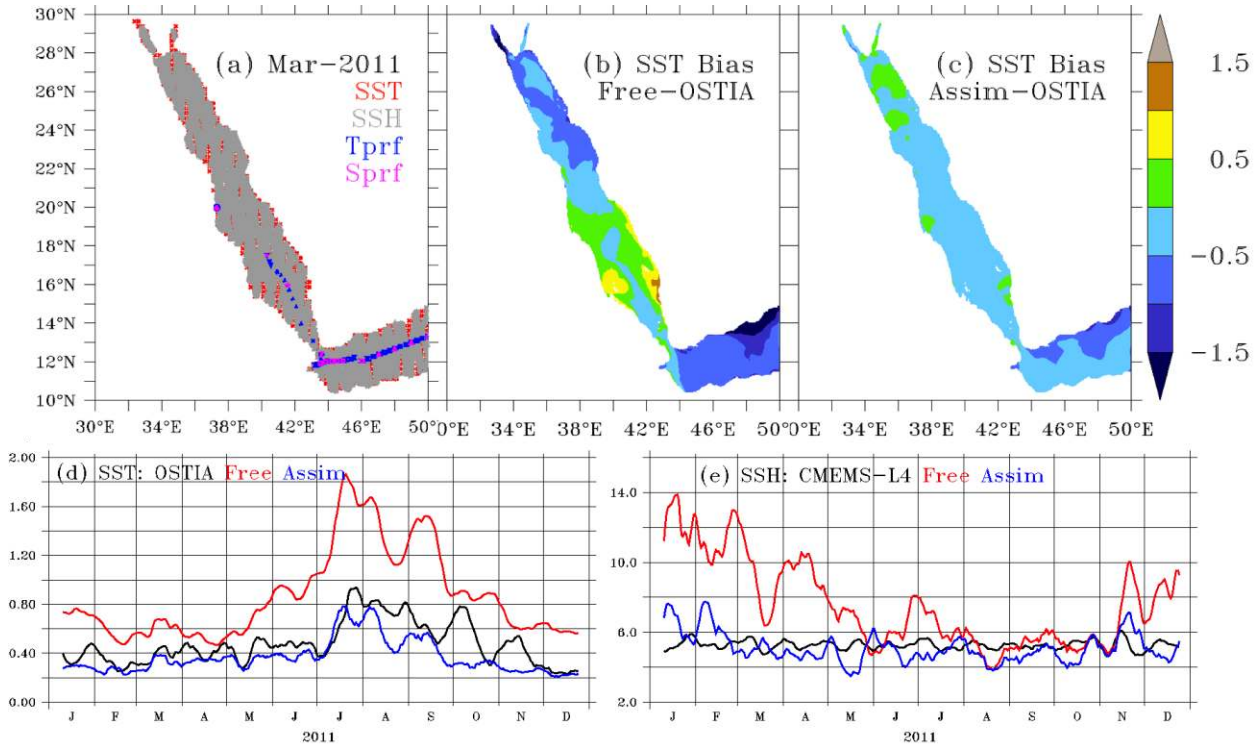

Figure 7. Impact of assimilation in the ensemble DART-MITgcm assimilation system. Panel (a) displays the spatial distribution of SST, SSH, and in-situ temperature and salinity observations that were assimilated in the DART-MITgcm ocean ensemble system during an arbitrary month (March 2011). The coverage of the regularly-spaced SST observations (red dots) is mostly masked by that of along-track SSH (grey dots) observations, which cover most of the Red Sea basin over a month period. Panels (b) and (c) respectively show the SST bias for free- and assimilative-model runs estimated over the period 1st March-31st December, 2011 with respect to OSTIA, a 5km resolution daily available interpolated level-4 gridded product generated by blending satellite and in situ observations of SST. Panels (d) and (e) respectively display time series of forecast RMSEs averaged over the model domain for SST (°C) and SSH (cm). Black, red and blue curves correspond to RMSEs of OSTIA for SST and CMEMS-L4 for SSH (daily available at 25km resolution), and free- and assimilative-model runs, respectively.

Accepted for publication in *Bulletin of the American Meteorological Society*. DOI 10.1175/BAMS-D-19-0005.1.

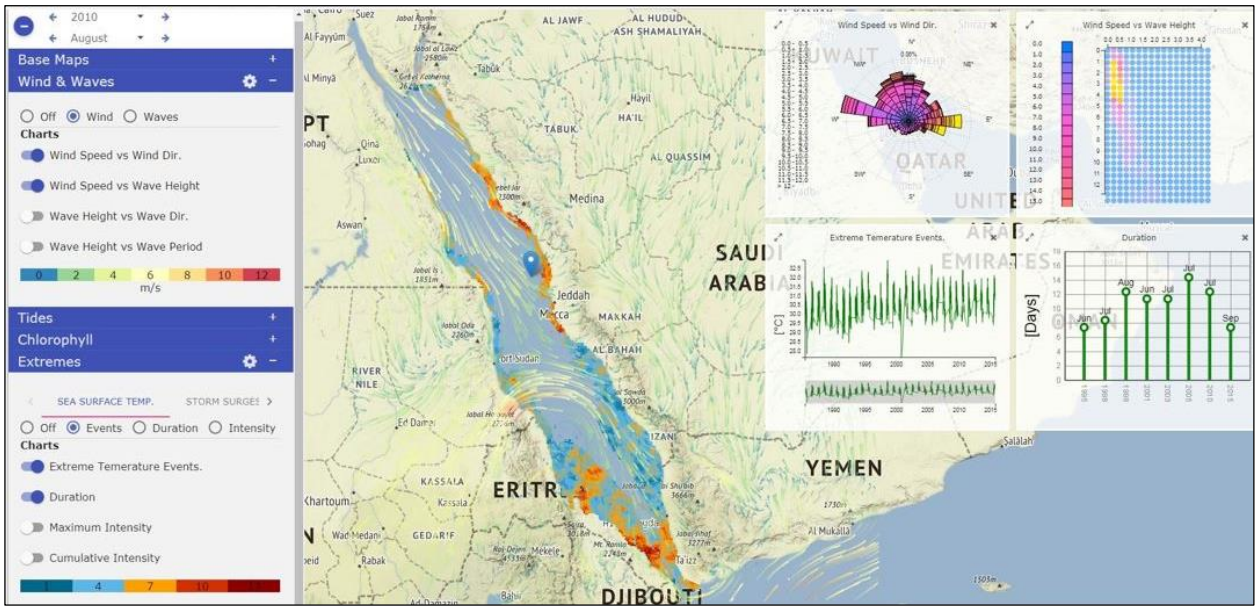

Figure 8. The 'RedSeaAtlas' system showing overall wind patterns and statistics (at the dropped pin location, here north of Jeddah in the central Red Sea) of extreme temperature events in the Red Sea. Users can select any region to show more detailed information and associated attributes through different charts (Afzal et al., 2019).

Accepted for publication in *Bulletin of the American Meteorological Society*. DOI 10.1175/BAMS-D-19-0005.1.

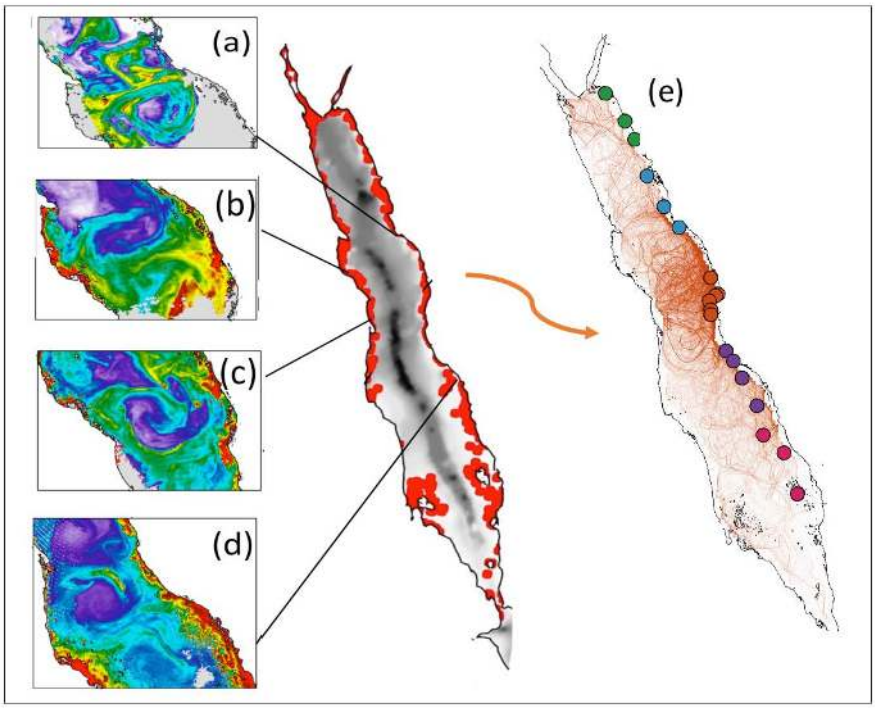

1075

1076 Figure 9. Remotely-sensed ocean colour observations portraying surface flow (eddies and
1077 currents) between coral reefs in the Red Sea. *Left panels* (a-d): Chlorophyll (mg/m3)
1078 patterns at different time periods (1-Jun-2010, 21-Jun-2009, 4-Mar-2006, and 13-Apr-
1079 2001) illustrating the impact of the basin-wide mesoscale variability on the basin
1080 productivity. The central map depicts sea-floor elevation and the position of coral reefs
1081 (red circles) in the Red Sea (coral reef positions were acquired from: Global Distribution
1082 of Coral Reefs, 2010). (e) Simulated particle dispersion trajectories forming pathways of
1083 connectivity in the Red Sea. Particles were released from the locations of the coral reefs
1084 along the east coast of the central Red Sea. The different colours denote each of the five
1085 different Red Sea provinces (Raitsos et al., 2013). The panel suggests basin-wide
1086 connectivity with the central Red Sea driven by mesoscale activity, except for the southern
1087 Red Sea which connects more with the Gulf of Aden (Raitsos et al., 2017; Wang et al.,
1088 2019).

Accepted for publication in *Bulletin of the American Meteorological Society*. DOI 10.1175/BAMS-D-19-0005.1.

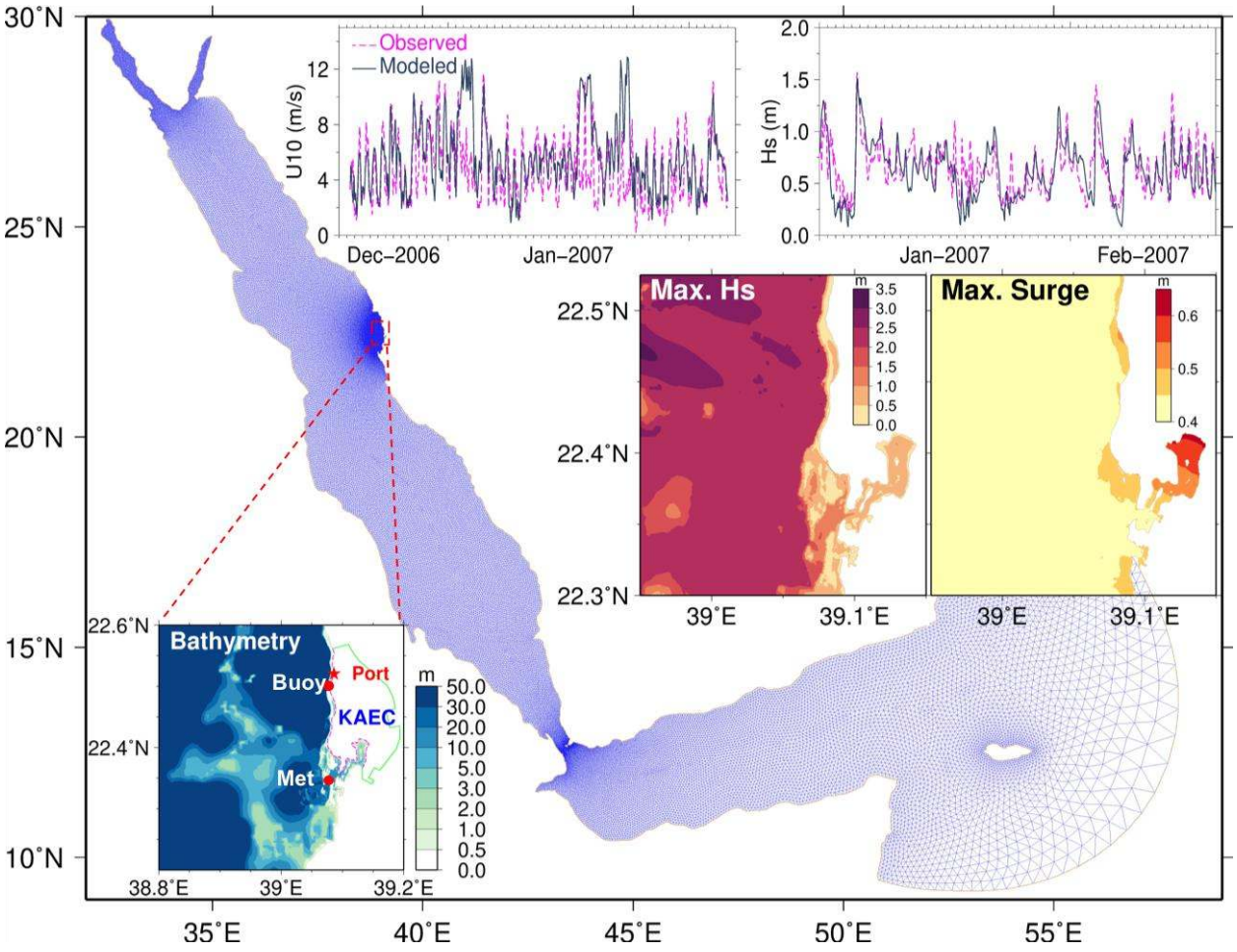

Figure 10. Coupled ADCIRC+SWAN model domain used for estimating extreme wave heights and water levels along the KAEC coastline. The unstructured grid resolution varies from 60 km near the boundary in the Arabian Sea to 60 m near the KAEC coastline. The bathymetry of the KAEC and maximum of significant wave heights and water levels from 30-year simulations are also shown in inset images. The model-data comparisons at the locations indicated in the Bathymetry plot (by Met for winds and Buoy for waves) suggest a good agreement between the model simulations and the measurements.

Accepted for publication in *Bulletin of the American Meteorological Society*. DOI 10.1175/BAMS-D-19-0005.1.

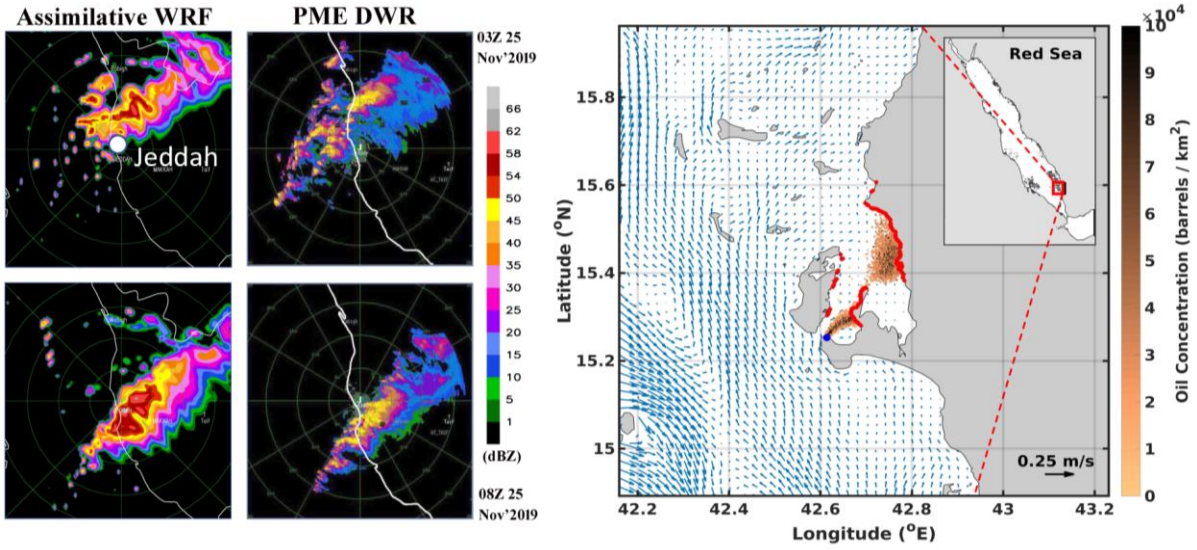

1100

1101 Figure 11. (a) Evolution of reflectivity as predicted by WRF with assimilation of conventional and
1102 satellite radiance data against PME DWR data during Jeddah extreme rainfall event at 0300
1103 UTC, and 0800 UTC on 25 November 2009 (Viswanadhapalli et al., 2016). (b)
1104 Concentration of oil (in barrels/km2) after 14 days of spill from the tanker location marked
1105 by the blue dot. Red dots indicate beached spill locations. The investigated region is
1106 indicated by the red box in the inserted Red Sea basin panel.

1107

Accepted for publication in *Bulletin of the American Meteorological Society*. DOI 10.1175/BAMS-D-19-0005.1.